Journal Pre-proof

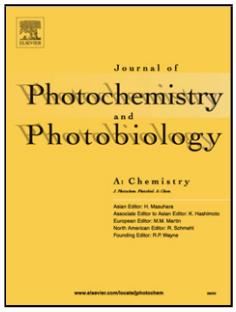

Shape controllable ultrasound assisted fabrication of $CaZrO_3:Dy^{3+}$ hierarchical structures for display, dosimetry and advanced forensic applications

D. Navami, G.P. Darshan, R.B. Basavaraj, S.C. Sharma, D. Kavyashree, K.N. Venkatachalaiah, H. Nagabhushana

PII: S1010-6030(19)31219-5

DOI: https://doi.org/10.1016/j.jphotochem.2019.112248

Reference: JPC 112248

To appear in: *Journal of Photochemistry & Photobiology, A: Chemistry*

Received Date: 18 July 2019

Revised Date: 20 September 2019

Accepted Date: 15 November 2019

Please cite this article as: Navami D, Darshan GP, Basavaraj RB, Sharma SC, Kavyashree D, Venkatachalaiah KN, Nagabhushana H, Shape controllable ultrasound assisted fabrication of $CaZrO_3:Dy^{3+}$ hierarchical structures for display, dosimetry and advanced forensic applications, *Journal of Photochemistry and amp; Photobiology, A: Chemistry* (2019), doi: https://doi.org/10.1016/j.jphotochem.2019.112248

Shape controllable ultrasound assisted fabrication of $CaZrO_3:Dy^{3+}$ hierarchical structures for display, dosimetry and advanced forensic applications

D. Navami[1], G.P. Darshan[2], R.B. Basavaraj[1], S.C. Sharma[3], D. Kavyashree[4], K. N. Venkatachalaiah[5], H. Nagabhushana[1,*]

[1]*Prof. C.N.R. Rao Centre for Advanced Materials Research, Tumkur University, Tumkur 572 103, India*
[2]*Department of Physics, Acharya Institute of Graduate Studies, Bangalore 560 107, India*
[3]*National Assessment and Accreditation Council, Bangalore 560 072, India (Work carried out as honorary Professor, Jain University, Bangalore 562 112, India)*
[4]*Department of Physics, Acharya Institute of Technology, Bangalore 560 107, India*
[5]*Department of Physics, Amrita School of Engineering, Amrita Vishwavidyapeetham, Amrita university, Bangalore 560 035, India*

*Corresponding author. Tel.: +91 9663177440, E-mail:bhushanvlc@gmail.com (H. Nagabhushana).

Graphical abstract

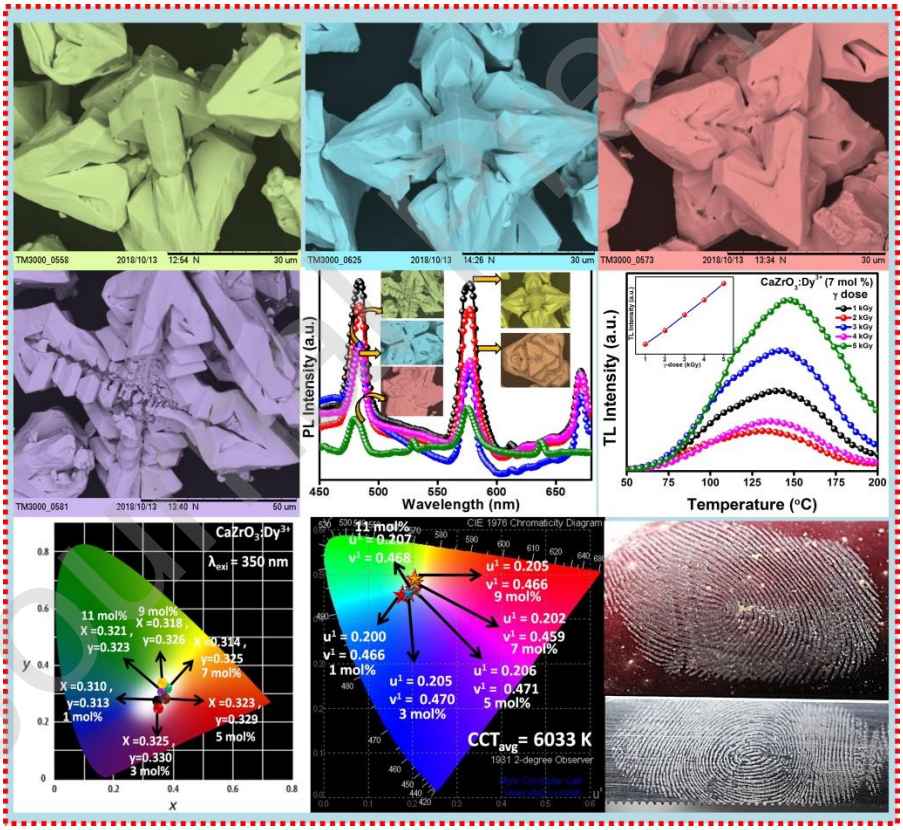

Research highlights

- Arrow-like $CaZrO_3:Dy^{3+}$ (1-11 mol %) hierarchical structures are fabricated via sonochemical route using *Aloe Vera* gel as a bio-surfactant.
- The structural and morphological studies are investigated in detail.
- Photometric properties apparent that, samples exhibit white color with high color purity.
- The optimized sample is used to visualize latent fingerprints on various surfaces.
- The prepared samples are highly useful for display device, dosimetry and forensic applications.

Abstract

Herein, we report hierarchical arrow-like structures of $CaZrO_3:Dy^{3+}$ (1-11 mol %) are prepared by sonochemical route using bio template as a surfactant. High purity and crystallinity of the product was obtained in sonochemical route when compared to conventional methods. Morphological results showed arrow-like structures which are highly reliant on many experimental parameters such as, sonication time, bio-template concentration, sonication power, pH and surfactant to water ratio. The photoluminescence emission spectra consist of sharp peaks at ~ 481 nm (blue), 575 nm (yellow) and 665 nm (red), which ascribed to $^4F_{9/2} \rightarrow {}^6H_{15/2}$, $^4F_{9/2} \rightarrow {}^6H_{13/2}$ and $^4F_{9/2} \rightarrow {}^6H_{11/2}$ transitions of Dy^{3+} ions, respectively. The decrement in the photoluminescence emission intensity after 7 mol % of Dy^{3+} ion concentration was clearly noticed, which may due to concentration quenching. The photometric properties of the prepared samples showed intense white emission with high color purity. Thermoluminescence glow curves of $CaZrO_3:Dy^{3+}$ (7 mol %) showed broad and intense peak at ~ 143 ^oC at a warming rate of 2 $^oCs^{-1}$. Thermoluminescence profile reveals the linear dependence with dose, least fading and highly reproducible. The optimized powders are employed to image the latent fingerprints with higher resolution on various porous, non-porous and semi-porous surfaces. The aforementioned results clearly indicate that the optimized hierarchical structures are effectively used in radiation dosimetry, display devices and advanced forensic applications.

Keywords: Sonochemical; Photoluminescence; Thermoluminescence; Photometric properties; Fingerprints.

1. Introduction

In recent years, there is a much need for the improvement of hierarchical structured (HS) luminescent powders with tailoring the optical properties under near ultra-violet (NUV) [1]. Rare earths (RE) ions doped in efficient hosts is treated as unique luminescent resources owing to their active connection with the nanotechnology for lighting and display devices fabrication [2-4]. The RE doped phosphors can tune their luminescence properties after altering the size and shape of the particles in nano regime. From the literature survey, it is evident that the preparation procedures can greatly impact on the morphology of the product. It has also been described that these materials can accomplish the essential energy related crunches [5]. The benefits of these HS are emerging day by day because of its excellent uses in display devices, optical temperature sensing, light emitting diodes (LEDs), sensors, etc. [6-8].

Hence, fabrication of highly luminescent HS with suitable dopant ions is essential. The materials with ABO_3 structures are motivating owing to its superior physical, chemical and optical properties [9]. As a member of perovskite ABO_3 family, $CaZrO_3$ was considered to be as an efficient host for doping lanthanide ions [10]. The $CaZrO_3$ structure consists of 3D sub-lattice of corner-connected ZrO_6 octahedron, in which Ca^{2+} locates in 8-fold coordination with O^{2-}. Further, it exhibits polymorphic transition from orthorhombic to cubic at 1750 °C [11]. At room temperature, its orthorhombic structure shows slightly deformed [ZrO_6] and [CaO_8] clusters, which may induce intermediate states in the energy gap of the material, affecting its optical properties. Such structural changes may induce some vacancy defects at the axial and planar oxygen sites of the [ZrO_6] octahedral [12]. It is well known that the vacancy defects may play important roles as not only carriers traps but also luminescence centers.

Thus, it is very essential for fabrication of $CaZrO_3$ HS with efficient route to fulfill the above pitfalls. Generally, the toxic solvents, harsh chemicals, additives and surfactants were used, but which are not eco-friendly. Hence to overcome from the eco-destructive routes, numerous efforts have been devoted towards green synthesis of metal-oxide nanoparticles using plant and animal extracts which contains protein chains, polysaccharides, bacteria, fungi, yeast, viruses etc. [13, 14]. Phytosynthesis was a beneficial and eco-friendly approach to prepare nanoparticles using plant extracts from its root, leaf, stem etc. The extracts of *Aloe Vera* (*A.V.*) plant gel was used as a bio-surfactant to achieve various nanomaterials. *A.V.* plant was a juicy plant belongs to the family of Liliaceae. *A.V.* gel contains 75 potentially active constituents: vitamins (including B1, B2, B3, B6, B12), enzymes, minerals (such as magnesium, calcium, potassium, phosphorus, sodium, manganese, zinc, copper, nitrogen, iron and chromium), sugars, salicylic acids, lignins, saponins, amino acids, alkaloids and flavones. The biological units such as polysaccharides, protein chains, enzymes etc. [15]. in the leaves of *A.V.* helps in various medical applications such as wound healing, antifungal activity, hypoglycemic, anticancer etc. Hence using *A.V.* plant gel as a bio-template helps in obtaining complex HS in the micro/nano level which has been improved the light emitting capacity compared to the other preparation routes. Till date, various synthesis routes were employed namely, combustion, sol-gel, hydrothermal, solid-state reaction, co-precipitation, etc. [16-23]. However, none of the above routes obtained HS, hence ultrasound assisted sonochemical method is utilized for tunable hierarchical morphology at very low temperature [24]. The process involved in ultrasound route is predominantly from acoustic cavitation, followed by the formation, growth and subsequent collapse of micro bubbles in a liquid. During cavitation process, the collapse of bubbles takes place as a result high temperature (> 5000 ^{o}C) and pressure (> 20 MPa) is achieved. These extreme conditions may result nano-sized particles

with HS. In addition, fast quenching rate, easy operation at ambient condition, high purity of the product are the major advantages of the ultrasonic method [25].

Thermoluminescence (TL) is also known as thermally stimulated luminescence (TSL) an effective tool for probing of electronic trap levels in phosphors, used in TL dosimetry for radiation detection [26]. TL is the light emitted by the phosphor which has been previously irradiated with ionizing radiations. In this phenomenon, the charge carriers (electrons and holes) trapped in luminescent centers when phosphor is irradiated to the radiation source [27]. The resulting emission is known as TSL, which is the emission of light achieved after warming the material. In order to use the phosphor material for dosimetric applications, it obeys linear dependency with dose, less fading, simple glow curve structure, superior sensitivity, etc. [28]. However, most of the phosphors do not follow these characteristics. Hence, suitable amalgamation of stable host, dopant and optimized luminescent centers are required. Till date numerous reports on TL studies of rare earth capped Zirconate phosphors are well documented in the literature [29]. However, a limited work has been carried out on photoluminescence (PL) and TL properties of $CaZrO_3$ HS prepared by bio-surfactant assisted sonochemical route.

Fingerprints (FPs) can offer distinctive evidence on persons and can extensively utilized in advanced forensic inquiries [30]. The ridge as well as furrow details of FPs give evidence on the donors owing to their precise and indisputable for each individual [31-37]. Generally, at crime sights, the FPs is not noticeable to the naked eyes. Hence, detailed practices are essential to discriminate the FPs [38]. Till date, a variety of powders namely, regular, metallic, and fluorescent tags are utilized for the visualization of LFPs [39]. Moreover, regular and metallic powders are not suitable due to their toxic in nature [40]. Hence, many efforts have been made to develop non-toxic, eco-friendly RE doped nanopowders (NPs) to visualize the latent fingerprints (LFPs). Generally, LFPs consists of

three types of ridge details (1-3) which are not well-recognized due to its diminished intensity of fluorescent powders. In order to overcome these difficulties, efficient luminescent HS are in urgent need. Till date, numerous techniques are proposed for the visualization of LFPs namely, powder dusting, ninhydrin, cyano acrylate fuming methods, etc. [41-43]. Among these methods, powder dusting method is simple and eco-friendly.

In this communication, various concentrations of Dy^{3+} (1-11 mol %) doped $CaZrO_3$ HS were synthesized by ultrasound assisted sonochemical method using *A.V* gel as a bio-template. The final product was well characterized by Powder X-ray diffraction (PXRD), Scanning electron microscope (SEM), Transmission electron microscope (TEM), Diffuse reflectance spectra (DRS), PL and TL. The optimized sample was utilized for forensic applications.

2. Experimental

2.1 Synthesis of $CaZO_3:Dy^{3+}$ (1-11 mol %) HS

The following chemicals are used for the synthesis of $CaZrO_3:Dy^{3+}$ without further purification. Calcium nitrate tetrahydrate [$Ca(NO_3)_2 \cdot 4H_2O$; 99.99 %, Sigma Aldrich], Zirconium (IV) oxynitrate hydrate [$ZrO(NO_3)_2 \cdot H_2O$; 99.99 %, Sigma Aldrich], Dysprosium (III) nitrate hexahydrate [$Dy(NO_3)_3.6H_2O$; 99.99 %, Sigma Aldrich]. The *A.V.* gel is used as bio-surfactant and the detailed extraction procedure is described elsewhere [15]. The appropriate quantities of precursors and bio-surfactant is dissolved well in double distilled water and stirred well using magnetic stirrer for ~ 30 min. The resultant mixture is transferred to 500 mL glass beaker, and then probe sonicator (Titanium made horn, with fixed frequency ~ 20 kHz, power ~ 300 W and temperature of ~ 50 ^oC) is introduced. The obtained precipitate at the end of the reaction is washed several times with alcohol and deionized water and then dried at ~ 80 ^oC overnight followed by calcination at ~ 800 ^oC for 3 h. Fig.1 shows the

schematic representation for the synthesis of Dy^{3+} doped $CaZrO_3$ HS by ultrasound assisted sonochemical method.

2.2. Characterization

The phase purity and crystallinity of the obtained product is studied using Shimadzu-7000 Powder X-ray diffractometer (Cu k_{α}, λ=1.54 Å). The morphological features are studied using Hitachi-3000 made SEM. Particle size and interplanar spacing (d) is studied by using TEM JOEL-TM-2100. DR of the product is measured using Perkin Elmer (Lamda-35) spectrophotometer. Through Jobin Yvon Spectroflourimeter Fluorolog-3 PL data were recorded. TL data were recorded using indigenous Nucleonix TL reader after irradiating γ-rays (^{60}Co) in the dose range 1-6 kGy.

3. Results and discussion

3.1. Structural analysis

The PXRD profiles of the $CaZrO_3$ HS calcined at various temperatures (500, 600, 700, 800 ^oC) were shown in Fig.2 (a). The mixed (cubic and orthorhombic) phase of samples calcined at ~ 500-700 ^oC was clearly noticed. Some weak peaks due to cubic phase of ZrO_2 are clearly observed with peak positions at ~ 30°, 35°, 50° and 60° (JCPDS no. 26-341) [44]. The intense diffraction peaks of the sample calcined at ~ 800 ^oC exhibit orthorhombic perovskite with space group Pcmn and well matches with JCPDS File No. 35-0790 of $CaZrO_3$ [45]. When the calcination temperature below ~ 800 °C, non-stoichiometric phase of $CaZrO_3$ is dominant. The PXRD patterns of $CaZrO_3$:Dy^{3+} (1-11 mol %) HS calcined at ~ 800 ^oC was shown in Fig. 2 (b). No obvious dopant Dy^{3+} ions peaks were noticed, indicating that the dopant Dy^{3+} ions were effectively substituted in the host $CaZrO_3$ sites. To authorize this, acceptable percentage ionic difference (D_r) between dopant and substituted cation is estimated using the relation [46];

$$Dr = \frac{R_h(CN) - R_d(CN)}{R_h(CN)} \text{ ----------(1)}$$

Here, R_h (CN); radius of host cation (R_{Ca}^{2+} = 1.12 Å) and R_d (CN); radius of dopant ion (R_{Dy}^{3+} = 1.027 Å). The D_r value was estimated and found to be ~ 8.30 % < 15 %. This clearly indicate that the Dy^{3+} ions successfully substituted the Ca^{2+} site in $CaZrO_3$:Dy^{3+} HS. However, the sample prepared in the absence of ultrasound (mechanically treated) also exhibit both non-stoichiometric $CaZrO_3$ phase, with cubic unit cell and orthorhombic phase (Fig.2 (c)).

The average crystallite size is calculated by utilizing both the Scherrer's and Williamson-Hall (W-H) method using the following relations [47];

$$D = \frac{0.9\lambda}{\beta \cos\theta} \text{ ----------(2)}$$

$$\beta = \frac{0.9\lambda}{D \cos\theta} + 4\varepsilon \tan\theta \text{ ----------(3)}$$

Here β; full width at half-maximum (FWHM), λ; wavelength of X-rays, θ; diffraction angle and ε; lattice strain. The W-H plots of $CaZrO_3$:Dy^{3+} (1-11 mol %) HS was shown in Fig. 2 (d). The average crystallite size (D) and lattice strain (ε) of the prepared HS are estimated and listed in Table 1.

Rietveld refinement is carried out using *FULLPROF* suit program [48] and the refined parameters are given in Table 2. The fitted PXRD profile of $CaZrO_3$:Dy^{3+} (5 mol %) is shown in Fig.2 (e). If the Goodness of fitting (χ^2) value is ~1, the refinement is considered to be good. In the present case, the value of χ^2 is ~1.39, suggesting that the refinement is within the acceptable limit. Further, by utilizing the refined values, the packing diagram of $CaZrO_3$:Dy^{3+} (5 mol %) is drawn using Diamond software and shown in Fig.2 (f).

3.2. Diffuse reflectance (DR) studies

The DR spectra of $CaZrO_3:Dy^{3+}$ (1-11 mol %) HS was shown in Fig.3 (a & b). The spectra consist of bands centered at ~ 298, 390, 796, 900 and 1085 nm, which attributed to the $^6H_{15/2} \rightarrow {}^4L_{19/2}$, $^6H_{15/2} \rightarrow {}^6I_{13/2}$, $^6H_{5/2} \rightarrow {}^6F_{5/2}$, $^6H_{5/2} \rightarrow {}^6F_{7/2}$ and $^6H_{5/2} \rightarrow {}^6F_{9/2} + {}^6H_{7/2}$ transitions of Dy^{3+} ions, respectively [49]. The Kubelka–Munk (K-M) theory [50] is employed to evaluate the energy band gaps (E_g) of $CaZrO_3:Dy^{3+}$ (1-11 mol %) HS (Fig. 3 (c)). The estimated E_g values are summarized in Table 1. From the table, the E_g values of the $CaZrO_3:Dy^{3+}$ (1-11 mol %) HS are found to be in the range of 5.74-5.87 eV. The obtained results are well matched with previously reported values [22].

3.3. Morphological analysis

In order to understand the formation mechanism of the 3D hierarchical $CaZrO_3:Dy^{3+}$ (7 mol %) various reaction parameters namely, effect of sonication time, surfactant concentration, sonication power, effect of pH and effect of surfactant to water ratio are studied. The effect of ultrasound irradiation time on the morphology is studied and shown in Fig.4. When the product achieved for ~ 1 h ultrasound irradiation time, exhibit a smooth triangle shaped plates with dip at the center (Fig.4 (a)). When irradiation time is increased to ~ 2 h, the dip at the center reduces without change in the surface smoothness of the plates (Fig.4 (b)). However, with further increase in ultrasound irradiation time to 3 h, triangular shaped dip as well as cracks are formed on the surface of the plates (Fig.4 (c)). With prolonged irradiation time (~ 4 h), cracks and dip at the center merge together to form star-like structure (Fig.4 (d)). When the ultrasound irradiation time is further increased to ~ 5 and 6 h, these star-like structures gets separated to form arrow-like morphology (Fig.4 (e, f)). However, when the irradiation time is extended to ~ 7 and 8 h, these cracks are appeared on each triangular plate and gets self-assembled to form 3D flower-like structures (Fig.4 (g & h)).

The effect of surfactant concentration on the morphology is also studied and depicted in Fig.5. When the *A.V.* gel concentration is ~ 5 mL, four armed sharp arrow-like structures are formed (Fig.5 (a)). However, when the surfactant *A.V.* gel concentration is increased to ~ 10 mL, short sharp arrow located on the top of the four armed arrows is observed (Fig.5 (b)). When the *A.V.* gel concentration is still increased to 15 mL, the length of the tip arrows is increased with reduction in length of the bottom arrows (Fig.5 (c)). When the *A.V.* gel concentration is ~ 20 mL, well-separated 3D arrows are observed (Fig.5 (d)). With further increase of *A.V.* gel concentration to ~ 25 mL, the lower portion of arrows gets splited apart with several cracks which results in flattened tip arrows (Fig.5 (e)). Finally, when the concentration is attained to 30 mL, these arrows gets joined together to form single 3D arrow-like structure (Fig.5 (f)). The absence of ultrasound treatment on the structure is studied and shown in Fig.5 (g & h). As can be seen from the figure, irregular flake-like structures are obtained, which clearly evidenced that ultrasound treatment plays a major role in obtained HS. The effect of sonication power on the morphology is also studied and shown in Fig.6. As can be seen from the figure, when the sonication power is ~ 20 and 22 kHz, three and four armed arrows with flattened surfaces are formed (Fig.6 (a & b)). When, sonication power is increased to ~ 24 kHz, four armed arrows with sharp edged surface are formed (Fig.6 (c)). However, when the sonication power is increased to ~ 26 and 28 kHz, small cracks on the surface of the arrows are observed (Fig.6 (d & e)). Sonication power is still increased to ~ 30 kHz, all the structures are found to be flattened with several cracks on the arrows (Fig.6 (f)).

Effect of pH on the morphology of the product is studied and depicted in Fig.7. When the pH of reaction solution is maintained to ~ 3, agglomerated flake-like structures are formed (Fig.7 (a)). When the pH is set to ~ 5, the self-assembled hierarchical arrow-like structures are obtained (Fig.7 (b)). Three armed arrows with cracks on the arms are observed when the pH is extended to ~ 7 (Fig.7 (c)). However, when the pH is ~ 9, four armed sharp arrows with

several solid blocks-like structures are formed (Fig.7 (d)). When the pH is increased to ~ 11 and 13, randomly oriented arrow-like structures were obtained, as shown in (Fig.7 (e & f)). The effect of bio- surfactant to water ratio on morphology is studied and shown in Fig.8. When the surfactant to water ratio is ~ 5/30 mL, solid blocks with sharp edges are formed (Fig. 8 (a)). When the ratio is ~10/30 mL, partial formation of arrows is obtained (Fig. 8 (b)). When the ratio become 15/30 mL, arrows with sharp edges gets oppositely directed to each other (Fig. 8 (c)). When the concentration of water is ~ 20/30 mL, well-resolved arrows with thick edges appeared (Fig. 8 (d)). However, when the surfactant to water ratio is increased to 25/30 mL, randomly oriented arrows with sharp tips are observed (Fig. 8 (e)). Sharp edged arrows oriented in reverse direction are obtained when the ratio is ~ 30/30 mL (Fig. 8 (f)).

Fig.9 shows the schematic representation of the various morphologies of $CaZrO_3:Dy^{3+}$ (7 mol %) HS under various sonochemical reaction conditions. Growth mechanism of various HS which include nucleation/growth, aggregation, self-assembly and Ostwald ripening. Amongst, Ostwald ripening plays a vital role to form 3D hierarchical nanostructures at the initial stage. After nucleation, particles will grow and start attaching continuously and bond to the other surface in an oriented direction. During Ostwald ripening, a tiny and unstable particles serve as sources for growth of large sized flakes with little surface energy [51, 52].

TEM image clearly evident that many arrows with length approximately lies in the range ~ 100-150 nm (Fig.10 (a)). From HRTEM image, the interplanar distance (d) corresponds to planes (121), (002) and (202) are estimated and found to be ~ 0.179, 0.284 and 0.399 nm, respectively (Fig.10 (b)). SAED patterns of the $CaZrO_3:Dy^{3+}$ (7 mol %) was shown in Fig.10 (c). The obtained fringes indicate that the product is highly nanocrystalline in nature. Fig.10 (d & e) shows the elemental composition of the prepared HS. The EDAX spectrum confirms the elements present in the sample and thereby it confirms the purity of the sample; however, the identified copper is due to grid used for TEM studies. Fig.10 (f & g) shows the TEM and

HRTEM images of the product obtained in the absence of ultrasound irradiation. It exhibits agglomerated particles and are matched with corresponding SEM images. The interplanar distance (d) was estimated and found to be ~ 0.41 and 0.38 nm.

3.4. PL studies

PL excitation spectrum of $CaZrO_3:Dy^{3+}$ (7 mol %) HS upon λ_{Emi} = 574 nm is shown in Fig.11 (a). The spectrum consists of several peaks located at ~ 324 ($^6H_{15/2}\rightarrow{}^6P_{3/2}$), ~ 350 ($^6H_{15/2}\rightarrow{}^6P_{7/2}$), ~ 385 ($^6H_{15/2}\rightarrow{}^4I_{13/2}$) and ~ 422 nm ($^6H_{15/2}\rightarrow{}^4G_{11/2}$) are due to f–f transition of Dy^{3+} ions [53]. The emission spectra upon excitation at ~ 350 nm comprises of peaks centered at ~ 481 nm (blue), 575 nm (yellow) and 665 nm (red), which ascribed to $^4F_{9/2}\rightarrow{}^6H_{15/2}$, $^4F_{9/2}\rightarrow{}^6H_{13/2}$ and $^4F_{9/2}\rightarrow{}^6H_{11/2}$ transitions of Dy^{3+} ions, respectively (Fig.11 (b)). Among, peak at ~ 481 nm is due to magnetic dipole transitions and are much less sensitive to the coordination environment. However, peak at ~ 575 nm belongs to a forced electric dipole transition, which is allowed only in the case that the Dy^{3+} ions are located at the local sites with non-inversion centre symmetry. The yellow emission is stronger than the blue emission, indicating that Dy^{3+} is located in more non centrosymmetric position in the $CaZrO_3$ host [54]. Variation of the PL intensity with different concentrations of Dy^{3+} ions is shown in inset Fig.11 (b)). It is evident that, the PL intensity is found to increase up to 7 mol %, and thereafter, it diminishes owing to concentration quenching phenomenon. The quenching process is mainly dependent on the cross relaxation mechanism resulting from resonance energy transfer between neighbouring Dy^{3+} ions. Considering the energy match rule, the following cross-relaxation channels (CRC) among Dy^{3+} are responsible for population decrease of $^4F_{9/2}$ level [55]:

CRC 1: $^4F_{9/2}\rightarrow{}^6H_{9/2}/{}^6F_{11/2} = {}^6H_{15/2}\rightarrow{}^6F_{3/2}$,

CRC 2: $^4F_{9/2}\rightarrow{}^6H_{7/2}/{}^6F_{9/2} = {}^6H_{15/2}\rightarrow{}^6F_{5/2}$,

CRC 3: $^4F_{9/2}\rightarrow{}^6F_{1/2} = {}^6H_{15/2}\rightarrow{}^6H_{9/2}/{}^6F_{11/2}$

When the excitation energy is transferred from a highly excited Dy^{3+} ion to a neighbouring Dy^{3+} ion and leads to transition from the ground state to the metastable level. The excited Dy^{3+} ions at $^4F_{9/2}$ level are de-excited through three cross-relaxation processes while the ground state Dy^{3+} ions will accept the energies from the Dy^{3+} at $^6H_{15/2}$ level simultaneously. Finally, all the Dy^{3+} ions will go in their ground states and thus the luminescence related to $^4F_{9/2}$ level is quenched [56]. Due to the smaller energy difference between the excited states, the population of the upper levels relaxed, non-radiative up to $^4F_{9/2}$, thereafter the ions relaxed radiative which results in 481 ($^4F_{9/2}\rightarrow{}^6H_{15/2}$), 575 ($^4F_{9/2}\rightarrow{}^6H_{13/2}$) and 665 nm ($^4F_{9/2}\rightarrow{}^6H_{11/2}$) transitions of the Dy^{3+} ions (Fig.11 (c)).

The concentration quenching is mainly caused by the non-radiative energy transfer among Dy^{3+} ions, which occurs as a result of an exchange interaction, radiation reabsorption, or a multipole–multipole interaction. The critical distance (R_c) between the neighbouring Dy^{3+} ion was estimated using Blasse's relation in order to know the type of the interaction mechanism [57];

$$R_c = 2\left(\frac{3V}{4\pi N X_c}\right)^{1/3} \text{----------(4)}$$

where X_c; 0.07 (optimal concentration), V; 455.322 $Å^3$ (volume of the unit cell), N: 4 (number of cations in the unit cell). By utilizing the above data, the value of R_c was estimated and found to be ~ 17.58 Å. This entails the electric multipolar interaction was mainly liable for the non-radiative energy transfer among the dopant Dy^{3+} ions in $CaZrO_3$:Dy^{3+} HS. For a better understanding of non-radiative energy transfer mechanism, the type of multipolar interactions, such as dipole–dipole (d–d), dipole–quadrupole (d–q) and quadrupole–quadrupole (q–q) involved in energy transfer was determined using following equation proposed by Dexter [58, 59];

$$\frac{I}{x} = K\left[1+\beta(x)^{Q/3}\right]^{-1} \text{----------(5)}$$

where *x*; activator concentration, *Q* = 3, 6, 8 and 10 indicates for d–d, d–q and q–q exchange interaction, respectively, *K* and *β*; constants for the same excitation condition for a given host crystal. The plot of log (I/x) over log(x) is shown in Fig.11 (d). By utilizing this plot slope of the curve is estimated and found to be -1.0993. Therefore, the Q value is found to be ~ 6.42 which is nearer to 6, indicating that dipole-dipole (d-d) interaction is responsible for the concentration quenching. In addition, PL emission spectra of various HS obtained at different sonochemical reaction parameters is studied and shown in Fig.11 (e). As can be seen from the figure, the highest PL intensity is recorded for arrow-like HS (20 mL *A.V.* concentration and 6 h duration).

The Commission Internationale de I′Eclairage (CIE) color coordinates (x, y) was key factor to examine the performance of the prepared HS [60]. Herein, the CIE color coordinates of the prepared $CaZrO_3:Dy^{3+}$ (1-11 mol %) HS were estimated and tabulated in Table 3. The obtained CIE values were close to the standard white light chromaticity coordinates (x=0.333 and y=0.333), signifying the higher white-light-emitting quality of the prepared HS. The CIE diagram of prepared $CaZrO_3:Dy^{3+}$ (1-11 mol %) HS was shown in Fig. 11 (f). It was evident that the CIE chromaticity coordinates are located in the pure white region of the CIE diagram, indicating that the prepared NPs can serve as a potential phosphor for wLEDs applications. In addition, the correlated color temperature (CCT) is estimated by transforming the CIE coordinates (x, y) of the light to (U_0, V_0) by using the following equations [61];

$$U_o = \frac{4x}{-2x + 12y + 3} \text{ ---------- (6)}$$

$$V_o = \frac{9y}{-2x + 12y + 3} \text{ ---------- (7)}$$

Generally, the CCT value > 5000 K considered as a cool white light, however the CCT value of < 5000 K can be reflected as warm white light [61]. CCT diagram of prepared

$CaZrO_3:Dy^{3+}$ (1-11 mol %) HS was shown in Fig. 11 (g). In the present work, the average CCT value was estimated and found to be ~ 6033 K, implying that the prepared HS was quite suitable for cool WLEDs application. Further, color purity of the $CaZrO_3:Dy^{3+}$ (1-11 mol %) HS were estimated using the equation [62];

$$color\quad purity = \frac{\sqrt{(x_s - x_i)^2 + (y_s - y_i)^2}}{\sqrt{(x_d - x_i)^2 + (y_d - y_i)^2}} \times 100\ \% \text{ ----------(8)}$$

where (x_d, y_d); chromaticity coordinates of the dominant wavelength, (x_s, y_s); coordinates of coordinates of the sample point and (x_i, y_i); white illuminate (x_i=0.33, y_i=0.33). The color purity of $CaZrO_3:Dy^{3+}$ (1-11 mol %) HS were estimated and found to be ~ 94 %. The overall results clearly indicate that the optimized HS finds potential applications in display devices.

3.5. TL studies

Fig.12 (a) shows the TL glow curves of 1kGy γ-irradiated $CaZrO_3$: Dy^{3+} (1-11 mol %) HS at a warming rate of 5 $^oCs^{-1}$. From the figure, it is evident that single well-resolved glow peak recorded at ~ 143 ^{o}C for all the Dy^{3+} doped samples. The highest TL intensity is registered for 7 mol % of Dy^{3+} doped samples and thereafter, it declines (Inset: Fig.12 (a)). In order to utilize the sample in radiation dosimetry, linearity with dose is essential parameter. Therefore, in order to test this, TL intensity with wide range of γ-doses (1-5 kGy) are studied and is shown in Fig.12 (b). From the figure it is clear that, TL intensity varies linearly up to 5 kGy γ-dose (Inset: Fig.12 (b)).

High surface to volume ratio is the main cause of linearity over wide range of dose. Several authors have explained the linearity construction on the track interaction model (TIM). Based on this model, when a TL dosimetry material is exposed to ionizing radiations (X-rays, gamma-rays and heavy ions) electron and hole pairs, are produced and penetrate through the phosphor material. Due to high energy radiations, the atoms displace in their tracks while transient through the phosphor besides ionizing it. Most of the charged particles

namely, electrons and holes trapped in the path of these ionizing radiations. Upon warming the phosphor material, the electrons and holes get freed from their respective positions and recombination takes place as result TL emission occur [63]. The charges gets vanishes non-radiatively if they miss to touch the luminescence centre (LC) by thermal or optical stimulation. The created traps by the ionizing radiation in a track depend on the cross- section as well as length of the tracks inside the phosphor. Hence, in a bulk material, greater energy radiation namely, γ-rays, β-rays or X-rays, can produce a track with length of the order of dimensions of the micro-crystallites while piercing through it. The probable order of the track is in the range of micrometer (μm) to millimetre (mm) or some nm depend upon their sizes. However, in the case of nanostructured (NS) materials, the track length is nearly few tenths of nanometers (nm). When compared to the number of LC or TC (trap centres) created in the HS, which is much less than that of bulk substance for the little doses. Conversely, as the given dose upsurges extra number of tracks is generated and get superimposed on one another which may not provide additional TL intensity as result saturation occur in the micron-sized materials.

A simple model has been proposed by various workers to explain the TL process in Dy^{3+} doped samples [64]. When the phosphor is exposed to γ-irradiation, holes and electrons are created. The holes are trapped at Dy^{4+} (hole center) and electrons are trapped at F^{+} center (electron center) [65];

$$Dy^{3+} + Hole \rightarrow Dy^{4+}$$

On thermal stimulation, the electron from electron centres (F^{+}) is released and recombines with the hole at the hole centres (Dy^{4+}). This recombination energy is transferred to (Dy^{3+}) luminescent centres, which further de-excite and give rise to TSL emission by following the mechanism below;

$$Dy^{4+} + electron \rightarrow Dy^{3+} + hv \rightarrow (Dy^{3+})^{*}$$

$$(Dy^{3+})^{*} \rightarrow Dy^{3+} + h\upsilon$$

TL glow curve structure is generally relies on warming rate (β) at which material is heated. Fig.12 (c) shows the TL glow peaks of $CaZrO_3:Dy^{3+}$ (7 mol %) irradiated with 5 kGy γ-dose at different warming rates (2-8 $^{o}Cs^{-1}$). As can be seen from the figure that, the decrement in glow peak intensity and peak shift with increasing β is clearly noticed. The peak shift is explained by the fact that at the lower heating rate the samples will be maintained at a certain temperature for a longer duration so that the traps become empty earlier resulting in a peak position in the low-temperature region [66]. However, the traps have insufficient time to get empty at the higher β, resulting in a higher peak temperature.

3.5.1. Computerized glow curve deconvolution (CGCD).

TL glow curve of $CaZrO_3:Dy^{3+}$ (7 mol %) HS irradiated with 6 kGy γ-dose at an warming rate of 2 $^{o}C/s$ (Fig.12 (d)). The TL glow curve exhibited a broad peak structure specifies that, it is a composition of more than one peak. Hence, CGCD method has been applied to distinct the each glow peaks. The mathematical equations as suggested by Kitis for I, II and general order given by [67];

For first order;

$$I(T) = I_m \exp\left[1 + \frac{E}{kT}\frac{T - T_m}{T_m} - \frac{T^2}{T_m^2}\exp\left(\frac{E}{kT}\frac{T - T_m}{T_m}\right)\left(1 - \frac{2kT_m}{E}\right) - \frac{2kT_m}{E}\right] \text{----------(9)}$$

For second order;

$$I(T) = 4I_m \exp\left(\frac{E}{kT}\frac{T - T_m}{T_m}\right)\left[\frac{T^2}{T_m^2}\exp\left(\frac{E}{kT}\frac{T - T_m}{T_m}\right)\left(1 - \frac{2kT_m}{E}\right) + 1 + \frac{2kT_m}{E}\right]^{-2} \text{----------(10)}$$

For general order;

$$I(T) = \text{Im}\; b^{\left(\frac{b}{b-1}\right)} \exp\left(\frac{E}{kT}\frac{T - T_m}{T_m}\right)\left[(b-1)\frac{T^2}{T_m^2}\left(1 - \frac{2kT}{E}\right)\exp\left(\frac{E}{kT}\frac{T - T_m}{T_m}\right) + 1 + \left(b - 1\frac{2kT_m}{E}\right)\right]^{-\frac{b}{b-1}} \text{------(11)}$$

where I(T); TL intensity, I_m; highest peak intensity, T_m; peak temperature, E; trap depth, b; order of kinetics and k; Boltzmann's constant. Likewise, the frequency factor 'S' is estimated by utilizing the equation [68];

$$S = \frac{\beta E}{kT_m^2}\exp\left(\frac{E}{kT_m}\right) \text{----------(12)}$$

The second and general order;

$$S = \frac{\beta E}{kT_m^2\left(1+(b-1)\frac{2kT_m^2}{E}\right)}\exp\left(\frac{E}{kT_m}\right) \text{----------(13)}$$

where β; linear heating rate.

The combination of experimental and deconvoluted TL glow peaks of $CaZrO_3:Dy^{3+}$ HS irradiated with 6 kGy γ-dose are depicted in Fig.12 (d). The deconvoluted TL glow peaks reveal the presence of four distinct glow peaks at 100, 113, 143 and 151ºC. In order to know the superiority of the fitted glow peaks Figure of Merit (FOM) is estimated using the relation [69];

$$FOM = \frac{\sum TL_{Exp} - TL_{The}}{\sum TL_{The}} \text{----------(14)}$$

where TL_{Exp}; TL intensity of experimental and TL_{The}; TL intensity of theoretical glow curves. The FOM values for $CaZrO_3:Dy^{3+}$ HS irradiated with 6 kGy γ-dose is found to be 1.63, 1.26, 1.54 and 1.34 for 2, 4, 6 and 8 $^oCs^{-1}$ heating rates, respectively. In the present study, the FOM is < 2 %, signifying that both experimental and theoretically achieved results are in good agreement. The estimated kinetic parameters are listed in Table 4 & 5.

3.5.2. Glow curve shape methods

To evaluate the kinetic parameters Chen's peak shape technique has been utilized. In this method, some necessary parameters such as maximum glow peak temperature (T_m), T_1 and T_2 are the temperatures corresponding to the half of the intensities on either side of the maximum of the glow peak. To evaluate the various kinetic parameters, the peak shape parameters such as total half intensity width $\omega = T_2 - T_1$; the high temperature half width $\delta = T_2 - T_m$; and the low temperature half width $\tau = T_m - T_1$ are to be determined.

In order to estimate the order of kinetics (b) the peak shape method is mainly used. The symmetry factor (μ_g) is estimated by utilizing the equation [70, 71];

$$\mu_g = \frac{\delta}{\omega} = \frac{T_2 - T_m}{T_m - T_1} \text{----------(15)}$$

where, δ and ω are expressed as $\delta = T_2 - T_m$, and $\omega = T_m - T_1$, respectively. The values of μ_g are 0.42 and 0.52 for first and second order kinetics, respectively. Secondly, another vital parameter (γ) suggested by Balarin gives the kinetic order as a function of the parameter [72];

$$\gamma = \frac{\delta}{\tau} = \frac{T_2 - T_m}{T_m - T_1} \text{----------(16)}$$

The value of γ ranges from 0.7 to 0.8 for the first order and it varies from 1.05 to 1.20 for the second order. Retrapping is negligible and the trap should be located near to the luminescent center in the case of first order. However, in the case of second order, the glow peaks are wider and more symmetric than the first order peak. The trap depth (E) values, frequency factor (S) and FOM of the glow curve of the $CaZrO_3:Dy^{3+}$ HS were estimated by various methods as described in the literatures [73, 74]. The estimated values were tabulated in Table 6.

3.5.3. Fading and reproducibility

The stability of the phosphor can be tested when the $CaZrO_3:Dy^{3+}$ (7 mol %) is stored up to 30 days (Fig.12 (e)). From the figure it is apparent that 18 % of TL fading is attained after 30 days of storage which demonstrating that the HS is quite useful for dosimetric applications. Reproducibility is another vital factor useful for the practical applications of phosphors in dosimetry [75]. A phosphor which is accepted as good TL dosimetry its sensitivity remains unchanged even after several cycles of exposures as well as readouts. The $CaZrO_3:Dy^{3+}$ (7 mol %) HS is tested for repeated cycles after γ- irradiated at 6 kGy. It is then rapidly cooled to RT and again irradiated to same γ-dose (6 kGy). Fig.12 (f) displays the results after four repetitive cycles of annealing irradiation-readout. The obtained results signify that the optimized powder can be reused several times in radiation rich areas.

4. LFPs visualization

The $CaZrO_3:Dy^{3+}$ (7 mol %) HS is used for visualization of LFPs. Thumb imprints are made on the various surfaces namely, porous (aluminum foil, plastic sheet, glass), non-porous (steel, granite, knife) and semi-porous (apple, leaf, tomato) surfaces respectively (Fig.13). In the present case the FPs taken from the single donor. The optimized powders are dusted on the respective surfaces with thumb imprints, and to eliminate the leftover powders an air blower is utilized for 30 s. The developed FPs are visualized and photographed under normal light (Fig.13). From the figure it is clear that, all the ridge features such as sharp ridges and valleys (base elements) individually detected on all the surfaces. Further, the type 1 (whorl), type 2 (long fork, dot, ridge end, hook and bridge) and type 3 (scar and sweat pores) clearly observed even on complex surfaces. The obtained results clearly revealed that, the optimized powders display promising characteristics for advanced forensic application.

5. Conclusions

A facile and effective ultrasonication route is used to fabricate $CaZrO_3:Dy^{3+}$ arrow-like hierarchical structures. This approach finds wide range benefits, namely straight forwardness, high efficiency, low cost and short time. Morphology is effectively engineered by varying experimental conditions, namely *A.V.* concentration, pH, ultrasound irradiation time, bio-surfactant to water ratio. Three characteristics PL emission peaks centered at 481 nm (blue), 575 nm (yellow) and 665 nm (red), which ascribed to $^4F_{9/2} \rightarrow {}^6H_{15/2}$, $^4F_{9/2} \rightarrow {}^6H_{13/2}$ and $^4F_{9/2} \rightarrow {}^6H_{11/2}$ transitions of Dy^{3+} ions, respectively. The cross-relaxation process is responsible for concentration quenching phenomena. The TL response of the HS irradiated with different γ- doses displays a linear behavior; simple glow curve structure, low fading and high reproducibility make the material a good candidate for radiation dosimetry, particularly for the calculation of high γ doses where the materials normally saturated. The optimized powders are effectively utilized for the visualization of LFPs on various porous, non-porous and semi-porous surfaces. The distinctive features of LFPs namely, long fork, ridge end, dot, hook, scar and sweat pores are detected. The obtained results clearly evident that, the suitability of the present HS in display, radiation dosimetry and advanced forensic applications.

Declaration of conflict of interest statement

The authors declare that they have no known competing financial interests or personal relationships that could have appeared to influence the work reported in this paper.

Acknowledgement

The author Dr. H Nagabhushana thanks VGST, Govt. of Karnataka, India [VGST/KFIST-4/GRD-489] for the sanction of this project.

References

[1] Jiayue Tian, Fangbo Zhang, Yu Han, Xi Zhao, Chunyan Chen, Cuimiao Zhang, Guang Jia, Template-directed synthesis, properties, and dual-modal bio-applications of multifunctional $GdPO_4$ hierarchical hollow spheres, Appl. Surf. Sci. 475 (2019) 264-272.
[2] P. Haritha, I.R. Martin, C.S. Dwaraka Viswanath, N. Vijaya, K. Venkata Krishnaiah, C.K. Jayasankar, D. Haranath, V. Lavin, V. Venkatramu, Structure, morphology and optical characterization of Dy^{3+}-doped $BaYF_5$ nanocrystals for warm white light emitting devices, Opt. Mater. 70 (2017) 16-24.
[3] R. Praveena, V. Sravani Sameera, P. Babu, Ch. Basavapoornima, C. K. Jayasankar, Photoluminescence properties of Ho^{3+}/Tm^{3+}-doped YAGG nano-crystalline powders, Opt. Mater. 72 (2017) 666-6720.
[4] A. Mraouefel, L. Guerbous, A. Boukerika, M. Diaf, A. Mendoud, M. Seraiche, M. Taibeche, M.S.E. Hamroun, N. Baadji, Effect of the vanadium concentration on structural and photoluminescence of $YP_{1-x}V_xO_4$: 1 at. % Tb^{3+} nanophosphors, Opt. Mater. 65 (2017) 129-136.
[5] Suninder Jeet, O. P. Pandey, The effect of templates on the morphological and optical properties of $BaMgAl10O_{17}$:Eu^{2+} phosphors, Vacuum, 161 (2019) 119-124.
[6] Tingting Jiang, Yongqian Wang, Dawei Meng, Xiuling Wu, Junxia Wang, Jieyu Chen, Controllable fabrication of CuO nanostructure by hydrothermal method and its properties, Appl. Surf. Sci., 311 (2014) 602-608.
[7] G.P. Darshan, H.B. Premkumar, H. Nagabhushana, S.C. Sharma, B. Umesh, R.B. Basavaraj, Nucleation and self-assembly dynamics of hierarchical $YAlO_3$:Ce^{3+} architectures: Nano probe for in vitro dermatoglyphics and anti-mimetic applications, Mat. Sci. & Eng. C, 99 (2019) 282–295.
[8] B.S. Shashikala, H.B. Premkumar, G.P. Darshan, H. Nagabhushana, S.C. Sharma, S.C. Prashantha, Rational design of bi-functional RE^{3+} (RE = Tb, Ce) and alkali metals (M^+ = Li, Na, K) co-doped $CaAl_2O_4$ nanophosphors for solid state lighting and advanced forensic applications, Mat. Res. Bul., 115 (2019) 88-97.
[9] Akanksha Maurya, A. Dwivedi, A. Bahadur, S.B. Rai, Enhanced upconversion and downshifting emissions from Tm^{3+}, Yb^{3+} co-doped $CaZrO_3$ phosphor in the presence of alkali ions (Li^+, Na^+ and K^+), J. Alloys and Comp., 786 (2019) 457-467.
[10] Wagner D. Macedo Jr., Agda E. Souza, Gleyson T.A. Santos, Silvio R.Teixeira, Elson Longo, Microwave-assisted hydrothermal synthesis followed by heat treatment: A new route to obtain $CaZrO_3$, Ceramic Int., 44 (2018) 953-958.
[11] S.G. Prasanna Kumar R. Hari Krishna, Nagaraju Kottam, P. Krishna Murthy, C. Manjunatha, R. Preetham, C. Shivakumara, TijuThomas, Understanding the photoluminescence behaviour in nano $CaZrO_3$:Eu^{3+} pigments by Judd-Ofelt intensity parameters, Dyes and Pig., 150 (2018) 306-314.
[12] D. Navami, R. B. Basavaraj, S. C. Sharma, B. Daruka Prasad, H. Nagabhushana, Rapid identification of latent fingerprints, security ink and WLED applications of $CaZrO_3$:Eu^{3+} fluorescent labelling agent fabricated via bio-template assisted combustion route, J. Alloys Compd. J. Alloys Compd. 762 (2018) 763-779.
[13] M. Dhanalakshmi, H. Nagabhushana, G.P. Darshan, B. Daruka Prasad, Ultrasound assisted sonochemically engineered effective red luminescent labeling agent for high resolution visualization of latent fingerprints, Mat. Res. Bul., 98 (2018) 250–264.
[14] J.C. Bünzli, Europium in the limelight, Nature Chem., 2 (2010) 696.

[15] G.P. Darshan, H.B. Premkumar, H. Nagabhushana, S.C. Sharma, B. Daruka Prasad, S.C. Prashantha, R.B. Basavaraj, Superstructures of doped yttrium aluminates for luminescent and advanced forensic investigations, J. Alloys and Compd., 686 (2016) 577-587.
[16] I.P. Sahu, D.P. Bisen, R.K. Tamrakar, K.V.R. Murthy, M. Mohapatra, Studies on the Luminescence Properties of $CaZrO_3:Eu^{3+}$ Phosphors Prepared by the Solid State Reaction Method, J. Sci.: Adv. Mater. Dev., 2 (2017) 69-78.
[17] Vijay Singh, S. Watanabe, T.K. Gundu Rao, Katharina Al-Shamery, Markus Haase, Young-Dahl Jho, Synthesis, characterisation, luminescence and defect centres in solution combustion synthesised $CaZrO_3:Tb^{3+}$ phosphor, J. Lumin., 132 (2012) 2036–2042.
[18] J. Huang, L. Zhou, Y. Lan, F. Gong, Q. Li, J. Sun, Synthesis and luminescence properties of the red phosphor $CaZrO_3:Eu^{3+}$ for white light-emitting diode application, Cent. Eur. J. Phys., 9 (2011) 975-979.
[19] I.L.V. Rosa, M.C. Oliveira, M. Assis, M. Ferrer, R.S. Andre, E. Longo, M.F.C. Gurgel, A theoretical investigation of the structural and electronic properties of orthorhombic $CaZrO_3$, Ceramic Int., 41 (2015) 3069–3074.
[20] J Le, L. N van Rij, R. C van Landschoot, J Schoonman, A wet-chemical method for the synthesis of in-doped $CaZrO_3$ ceramic powders, J. Eur. Ceram. Soc., 19 (1999) 2589-2591.
[21] Qiao Chen, Yongqian Wang, Mingyan Zheng, Hao Fang, Xiang Meng, Nanostructures confined self-assembled in biomimetic nanochannels for enhancing the sensitivity of biological molecules response, J. Mat. Sci.: Mat. in Ele., 29 (2018) 19757–19767.
[22] D. Navami, R.B. Basavaraj, G.P. Darshan, Hajeebaba K. Inamdar, S.C. Sharma, H.B. Premkumar, H. Nagabhushana, Evolution of shapes and identification of level II and III features of fingerprints using $CaZrO_3:Sm^{3+}$ fluorescent markers prepared via solution combustion route, Opt. Mat., 88 (2019) 479-487.
[23] Yongqian Wang, Tingting Jiang, Dawei Meng, Jun Yang, Yinchang Li, Qun Ma, Jun Han, Fabrication of nanostructured CuO films by electrodeposition andtheir photocatalytic properties, App. Sur. Sci., 317 (2014) 414–421.
[24] H.S. Sudheendra, G.P. Darshan, R.B. Basavaraj, Yashwanth V. Naik, H.B. Premakumar, H. Nagabhushana, J.F. Williams, K. Hareesh, M.K. Kokila, Influence of Zn^{2+} doping on the lattice defects and photoluminescence studies of $Sr_2CeO_4:Eu^{3+}$ nanophosphor: Applications for data encryption strategies, Opt. Mat., 90 (2019) 159-171.
[25] R. B. Basavaraj, G. P. Darshan, B. Daruka Prasad, S. C. Sharma, H. Nagabhushana, Rapid visualization of latent fingerprints using novel $CaSiO_3:Sm^{3+}$ nanophosphors fabricated via ultrasound route, J. Rare Earths, 37 (2019) 32-44.
[26] Sunil Thomas, J.M. Kalita, M.L. Chithambo, O.M. Ntwaeaborwa, The influence of dopants on thermoluminescence of $Sr_2MgSi_2O_7$, J. Lumin., 208 (2019) 104-107.
[27] Serdar Delice, Mehmet Isik, Nizami M. Gasanly, Low temperature thermoluminescence of Gd_2O_3 nanoparticles using various heating rate and $T_{max} - T_{exc}$ methods, Res. Phys. 12 (2019) 1809-1813.
[28] Karan Gupta, R.M. Kadam, N.S. Dhoble, S.P. Lochab, Vijay Singh, S.J. Dhoble, Photoluminescence, thermoluminescence and evaluation of some parameters of Dy^{3+} activated $Sr_5(PO_4)_3F$ phosphor synthesized by sol-gel method, J. Alloys Compd., 688 (2016) 982–993.
[29] G. Nag Bhargavi, Ayush Khare, Namita Brahme, Structural characterization and thermoluminescence studies of UV irradiated and Eu^{3+} activated $BaZr_{0.25}Ti_{0.75}O_3$ powders, Mater. Sci. Semicond. Process, 44 (2016) 38-47.

[30] C.J. Shilpa, R.B. Basavaraj, G.P. Darshan, H.B. Premkumar, S.C. Sharma, H. Nagabhushana, New insights into the rapid deposition and visualization of latent fingerprints: Cyan light emitting $GdAlO_3:Ce^{3+}$ nano fluorescent probe, J. Photochem. & Photo. A: Chem., 376 (2019) 288–304.
[31] R.B. Basavaraj, H. Nagabhushana, G.P. Darshan, B. Daruka Prasad, M. Rahul, S.C. Sharma, R. Sudaramani, K.V. Archana, Red and green emitting CTAB assisted $CdSiO_3:Tb^{3+}/Eu^{3+}$ nanopowders as fluorescent labeling agents used in forensic and display applications, Dyes Pigm., 147 (2017) 364-377
[32] G.P. Darshan, H.B. Premkumar, H. Nagabhushana, S.C. Sharma, S.C. Prashantha, B. Daruka Prasad, Effective fingerprint recognition technique using doped yttrium aluminate nano phosphor material, J. Colloid Inter. Sci. 464 (2016) 206-218.
[33] R.B. Basavaraj, H. Nagabhushana, G.P. Darshan, B. Daruka Prasad, S.C. Sharma, K.N. Venkatachalaiah, Ultrasound assisted rare earth doped Wollastonite nanopowders: Labeling agent for imaging eccrine latent fingerprints and cheiloscopy applications, J. Ind. Eng. Chem., 51 (2017) 90-105.
[34] M. Dhanalakshmi, H. Nagabhushana, R.B. Basavaraj, G. P. Darshan, B. Daruka Prasad, Surfactant-assisted $BaTiO_3:Eu^{3+}@SiO_2$ core–shell superstructures obtained by ultrasonication method: Dormant fingerprint visualization and red component of white light-emitting diode applications, ACS Sustainable Chem. Eng., 6 (2018) 5214–5226.
[35] A. Sandhyarani, M.K. Kokila, G.P. Darshan, R.B. Basavaraj, B. Daruka Prasad, S.C. Sharma, T.K.S. Lakshmi, H. Nagabhushana, Versatile core-shell $SiO_2@SrTiO_3:Eu^{3+}$, Li^+ nanopowders as fluorescent label for the visualization of latent fingerprints and anti-counterfeiting applications, Chem. Eng., J. 327 (2017) 1135-1150.
[36] M. Wang, M. Li, M. Yang, X. Zhang, A. Yu, Y. Zhu, P. Qiu, C. Mao, NIR-induced highly sensitive detection of latent fingermarks by $NaYF_4$: Yb, Er upconversion nanoparticles in a dry powder state, Nano Res., 8 (2015) 1800–1810.
[37] N. H. Deepthi, G. P. Darshan, R. B. Basavaraj, B. Daruka Prasad, H. Nagabhushana, Large-scale controlled bio-inspired fabrication of 3D $CeO_2:Eu^{3+}$ hierarchical structures for evaluation of highly sensitive visualization of latent fingerprints, Sens. Act. B: Chem., 255 (2018) 3127-3147.
[38] K.N. Venkatachalaiah, H. Nagabhushana, R.B. Basavaraj, G.P. Darshan, B. Daruka Prasad, S.C. Sharma, Flux blended synthesis of novel $Y_2O_3:Eu^{3+}$ sensing arrays for highly sensitive dual mode detection of LFPs on versatile surfaces, J. Rare Earths, 36 (2018) 954-964.
[39] C. Suresh, H. Nagabhushana, G.P. Darshan, R.B. Basavaraj, D. Kavyashree, S.C. Sharma, A. Arulmozhi, B. Daruka Prasad, H.J. Amith Yadav, Facile $LaOF:Sm^{3+}$ based labeling agent and their applications in residue chemistry of latent fingerprint and cheiloscopy under UV visible light, Arabian J. Chem., 11 (2018) 460-482.
[40] H.S. Yogananda, R.B. Basavaraj, G.P. Darshan, B. Daruka Prasad, Ramachandra Naik, S.C. Sharma, H. Nagabhushana, New design of highly sensitive and selective $MoO_3:Eu^{3+}$ micro-rods: Probing of latent fingerprints visualization and anti-counterfeiting applications, J. Colloid Interface Sci., 528 (2018) 443-456.
[41] B. Marappa, M.S. Rudresha, R.B. Basavaraj, G.P. Darshan, B. Daruka Prasad, S.C. Sharma, S. Sivakumari, P. Amudha, H. Nagabhushana, EGCG assisted $Y_2O_3:Eu^{3+}$ nanopowders with 3D micro-architecture assemblies useful for latent finger print recognition and anti-counterfeiting applications, Sen. Act. B: Chem., 264 (2018) 426-439.
[42] S. Yeshodamma, D.V. Sunitha, R.B. Basavaraj, G.P. Darshan, B. Daruka Prasad, H. Nagabhushana, Monovalent ions co-doped $SrTiO_3:Pr^{3+}$ nanostructures for the visualization of latent fingerprints and can be red component for solid state devices, J. Lumin., 208 (2019) 371-387.

[43] M. Dhanalakshmi, R. B. Basavaraj, G. P. Darshan, S. C. Sharma, H. Nagabhushana, Pivotal role of fluxes in $BaTiO_3:Eu^{3+}$ nano probes for visualization of latent fingerprints on multifaceted substrates and anti-counterfeiting applications, Microchem. J., 145 (2019) 226-234.
[44] Akanksha Maurya, A. Dwivedi, A. Bahadur, S. B. Rai, Enhanced upconversion and downshifting emissions from Tm^{3+}, Yb^{3+} co-doped $CaZrO_3$ phosphor in the presence of alkali ions (Li^+, Na^+ and K^+), J. Alloys Compd., 786 (2019) 457-467.
[45] B. Evangeline, P. Abdul Azeem, R. Prasada Rao, G. Swati, D. Haranath, Structural and luminescent features of cerium doped $CaZrO_3$ blue Nanophosphors, J. Alloys Compd., 705 (2017) 618-623.
[46] G.P. Darshan, H.B. Premkumar, H. Nagabhushana, S.C. Sharma, S.C. Prashantha, H.P. Nagaswarupa, B. Daruka Prasad, Blue light emitting ceramic nano-pigments of Tm^{3+} doped $YAlO_3$: Applications in latent finger print, anti-counterfeiting and porcelain stoneware, Dyes & Pig. 131 (2016) 268-281.
[47] G.P. Darshan, H.B. Premkumar, H. Nagabhushana, S.C. Sharma, B. Daruka Prasad, S.C. Prashantha Neodymium doped yttrium aluminate synthesis and optical properties - A blue light emitting nanophosphor and its use in advanced forensic analysis, Dyes Pigm., 134 (2016) 227-233.
[48] Xue Yang, Quanjun Li, Ran Liu, Bo Liu, Shuqing Jiang, Ke Yang, Jing Liu, Zhiqiang Chen, Bo Zou, Tian Cui, Bingbing Liu, A novel pressure-induced phase transition in $CaZrO_3$, Cryst. Eng. Comm., 16 (2014) 4441.
[49] A.K. Bedyal, Vinay Kumar, Ram Prakash, O.M. Ntwaeaborwa, H.C. Swart, A near-UV-converted $LiMgBO_3:Dy^{3+}$ nanophosphor: Surface and spectral investigations, App. Sur. Sci., 329 (2015) 40-46.
[50] M. Mangalagowri, R.B. Basavaraj, G.P. Darshan, M.S. Raju, Yashwanth V. Naik, D. Kavyashree, Hajeebaba K. Inamdar, S.C. Sharma, H. Nagabhushana, Sonochemical synthesis of green emitting $Ca_2SiO_4:Er^{3+}$ nanopowders: Promising applications in optical thermometry and radiation dosimeter, Opt. Mat., 92 (2019) 125–135.
[51] B.S. Rohini, H. Nagabhushana, G.P. Darshan, R.B. Basavaraj, S.C. Sharma, P. Amudha, M. Rahul, B. Daruka Prasad, Multifunctional applications of self - Assembled 3D CeO_2: Cr^{3+} hierarchical structures synthesized via ultrasound assisted sonochemical route, J. Alloys Compd., 724 (2017) 897-909.
[52] M. Venkataravanappa, H. Nagabhushana, B. Daruka Prasad, G.P. Darshan, R.B. Basavaraj, G.R. Vijayakumar, Dual color emitting Eu doped strontium orthosilicate phosphors synthesized by bio-template assisted ultrasound for solid state lightning and display applications, Ultrason. Sonochem., 34 (2017) 803-820.
[53] Q. Liu, Y. Liu, Z. Yang, Y. Han, X. Li, G. Fu, Multi-wavelength excited white-emitting phosphor Dy^{3+}-activated $Ba_3Bi(PO_4)_3$, J. Alloys Compd., 515 (2012) 6-19.
[54] M. Venkataravanappa, R.B. Basavaraj, G.P. Darshan, B. Daruka Prasad, S.C. Sharma, P. Hema Prabha, S. Ramani, H. Nagabhushana, Multifunctional Dy (III) doped di-calcium silicate array for boosting display and forensic applications, J. Rare Earths, 36 (2018) 690-702.
[55] S. Dutta, S. Som, S. K. Sharma, Luminescence and photometric characterization of K^+ compensated $CaMoO_4:Dy^{3+}$ nanophosphors, Dalton Trans., 42 (2013) 9654-9661.
[56] S. Dutta, S. Som, S. K. Sharma, Excitation spectra and luminescence decay analysis of K^+ compensated Dy^{3+} doped $CaMoO_4$ phosphors, RSC Adv., 5 (2015) 7380-7387.
[57] G. Blasse, B.C. Grabmaier, *Luminescent Materials*, Springer, Verlag, 1994.
[58] G. Blasse, Energy transfer in oxidic phosphors, Phys. Lett., A 28 (1968) 444–445.
[59] D.L. Dexter, A theory of sensitized luminescence in solids, J. Chem. Phys. 21(1953) 836–850.

[60] Publication CIE no 17.4 (1987) International Lighting Vocabulary, Central Bureau of the Commission Internationale de L 'Eclairage, Vienna, Austria.
[61] A.S. Rajashekharaiah, G.P. Darshan, R.B. Basavaraj, Yashwanth V. Naik, D. Kavyashree, S.C. Sharma, H. Nagabhushana, NUV light-induced visible green emissions of Erbium-doped hierarchical $Bi_2Zr_2O_7$ structures, Opt. Mat., 95 (2019) 109237.
[62] K.R. Venkatesha
Babu, C.G. Renuka, R.B. Basavaraj, G.P. Darshan, H. Nagabhushana, One pot synthesis of $TiO_2:Eu^{3+}$ hierarchical structures as a highly specific luminescent sensing probe for the visualization of latent fingerprints, J. Rare Earths, 37 (2) (2018) 134-144.
[63] V. Chopra, S. J. Dhoble, Karan K. Gupta, A. Singh, A. Pandey, Thermoluminescence of $Li_2B_4O_7$:Cu phosphor exposed to proton beam for dosimetric application, Radiat. Meas., 118 (2018) 108-115.
[64] Jyoti Singh J. Manam Fouran Singh, Synthesis and thermoluminescence studies of γ-irradiated Dy^{3+} doped $SrGd_2O_4$ phosphor, Mat. Res. Bul., 94 (2017) 113-121.
[65] Pradeep Dewangan, D.P. Bisen, Nameeta Brahme, Shweta Sharma, Structural characterization and luminescence properties of Dy^{3+} doped $Ca_3MgSi_2O_8$ phosphors, J. Alloys Compd., 777 (2019) 423-433.
[66] M. Chowdhury, S.K. Sharma, S.P. Lochab, Thermoluminescence glow curve analysis of γ-irradiated Eu^{3+} doped SnO_2 composites, Ceram. Int., 42 (2016) 5472-5478.
[67] F. Ortega, M. Santiago, N. Martinez, J. Marcazzo, P. Molina, E. Caselli, On the analysis of glow curves with the general order kinetics: Reliability of the computed trap parameters, J. Lumin.184 (2017) 38-43.
[68] Arun Kumar, Arvind Kumar, Rakesh Dogra, Mohit Manhas, Sandeep Sharma, Ravi Kumar, Investigation of thermoluminescence and kinetic parameters of gamma ray exposed LiF: Sm^{3+}, Eu^{3+} nanophosphors for dosimetric applications, Ceram. Int. 44 (2018) 15535-15541.
[69] Karan Gupta, R.M. Kadam, N.S. Dhoble, S.P. Lochab, Vijay Singh, S.J. Dhoble, Photoluminescence, thermoluminescence and evaluation of some parameters of Dy^{3+} activated $Sr_5(PO_4)_3F$ phosphor synthesized by sol-gel method, J. Alloys Compd. 688 (2016) 982–993.
[70] S. Delice, M. Isik, N. M. Gasanly, Characterization of trap centers in Gd_2O_3 nanoparticles by low temperature thermoluminescence measurements, Optik. 158 (2018) 237-242.
[71] S. Jayasudha, K. Madhukumar, C.M.K. Nair, Resmi G. Nair, S. Rajesh, T.S. Elias, V.M. Anandakumar, N. Gopakumar, TL dosimetric characterization of gamma irradiated $SrSO_4$:Eu phosphors, J. Lumin., 183 (2017) 259–265.
[72] A. M. Sadek, H. M. Eissa, A. M. Basha, G. Kitis, Resolving the limitation of the peak fitting and peak shape methods in the determination of the activation energy of thermoluminescence glow peaks J. Lumin., 146 (2014) 418-423.
[73] Mehmet Oglakci, Sibel Akça, Yusuf Ziya Halefoglu, Tamer Dogan, Mehmet Ayvacikli, Yüksel Karabulute, Mustafa Topaksu, Nurdogan Can, Characterization and thermoluminescence behavior of beta irradiated $NaBaBO_3$ phosphor synthesized by combustion method, Ceramic Int., 45 (2019) 7011-7017.
[74] Ahmed Kadari, Serdar Delice, Nizami Mamed Gasanly, Dose dependence effect of thermoluminescence process in $TlInS_2$:Nd single crystals, Optik, 138 (2017) 372-376.
[75] P. Page, R. Ghildiyal, K.V.R. Murthy, Photoluminescence and thermoluminescence properties of $Sr_3Al_2O_6:Tb^{3+}$, Mater. Res. Bull., 43 (2008) 353–360.

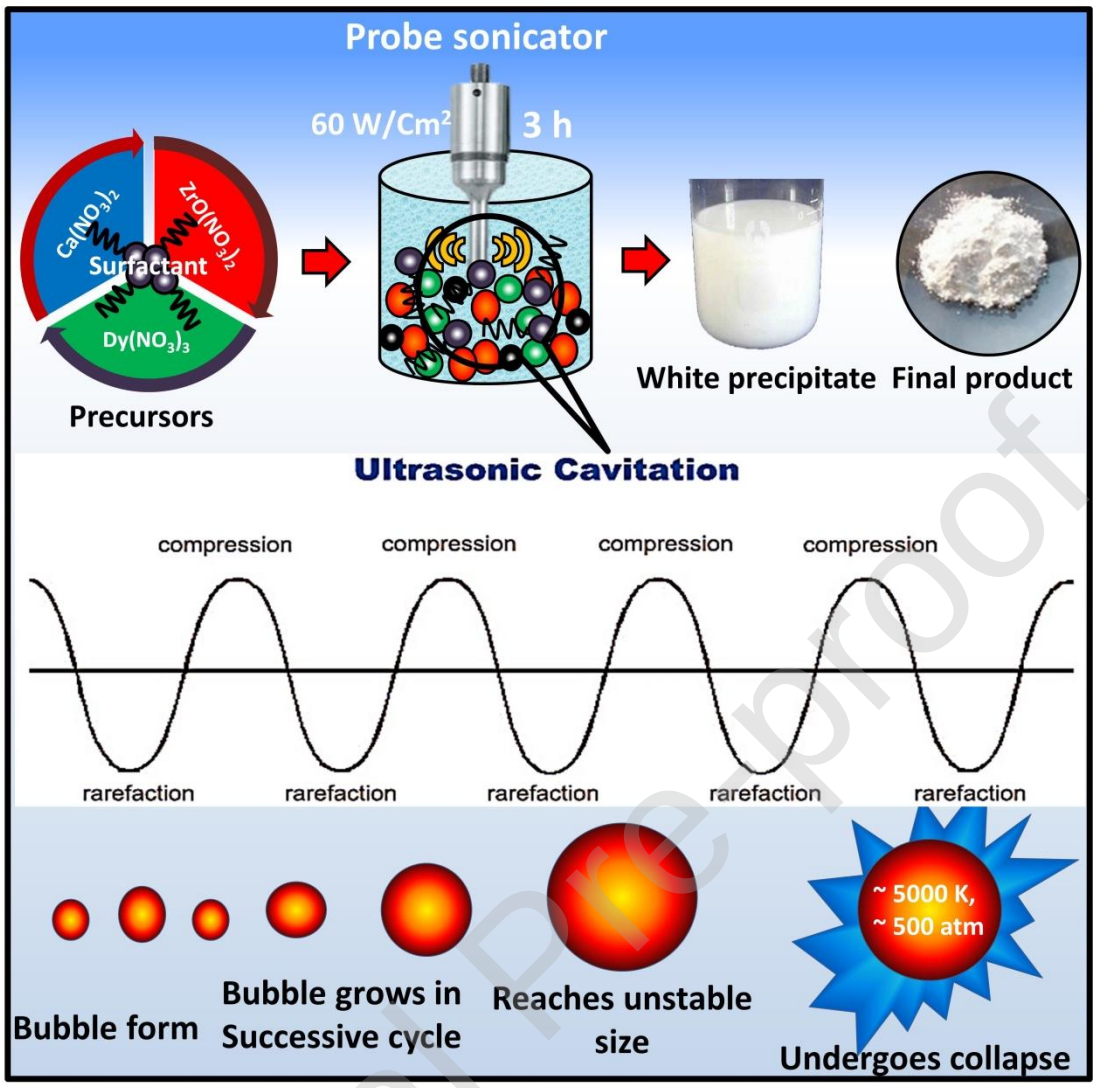

Fig.1. Schematic representation of sonochemical synthesis of $CaZrO_3:Dy^{3+}$ HS.

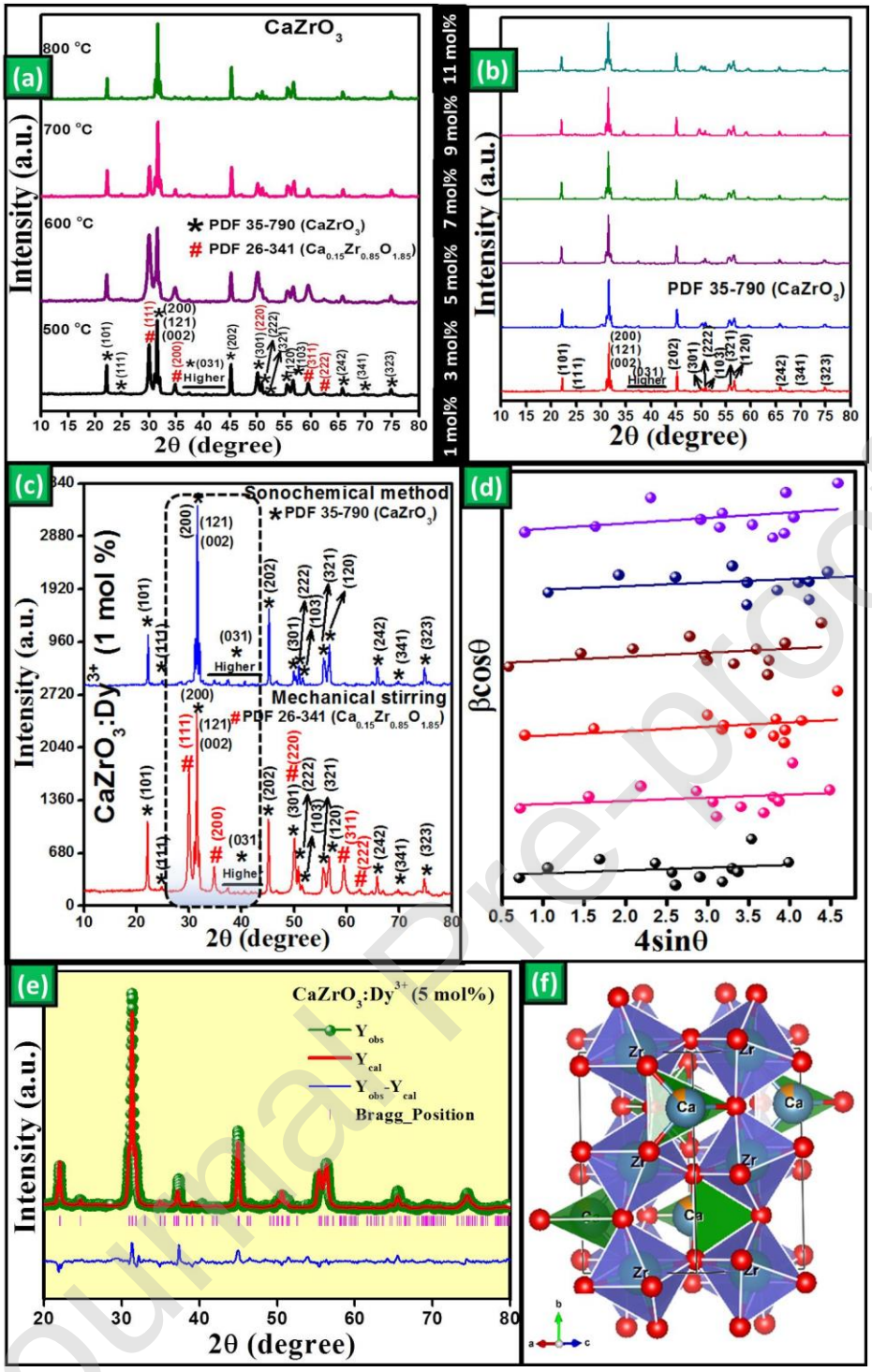

Fig.2. PXRD profiles of (a) $CaZrO_3$ with different calcination temperatures (500-800 ^oC), (b) $CaZrO_3:Dy^{3+}$ (1-11 mol %) calcined at 800 ^oC. (c) comparison between the sonochemical and mechanically prepared $CaZrO_3$ calcined at 800 ^oC, (d) W-H plots of $CaZrO_3:Dy^{3+}$ (1-11 mol %), (e & f) Rietveld refinement and packing diagram of $CaZrO_3:Dy^{3+}$ (5 mol %) HS.

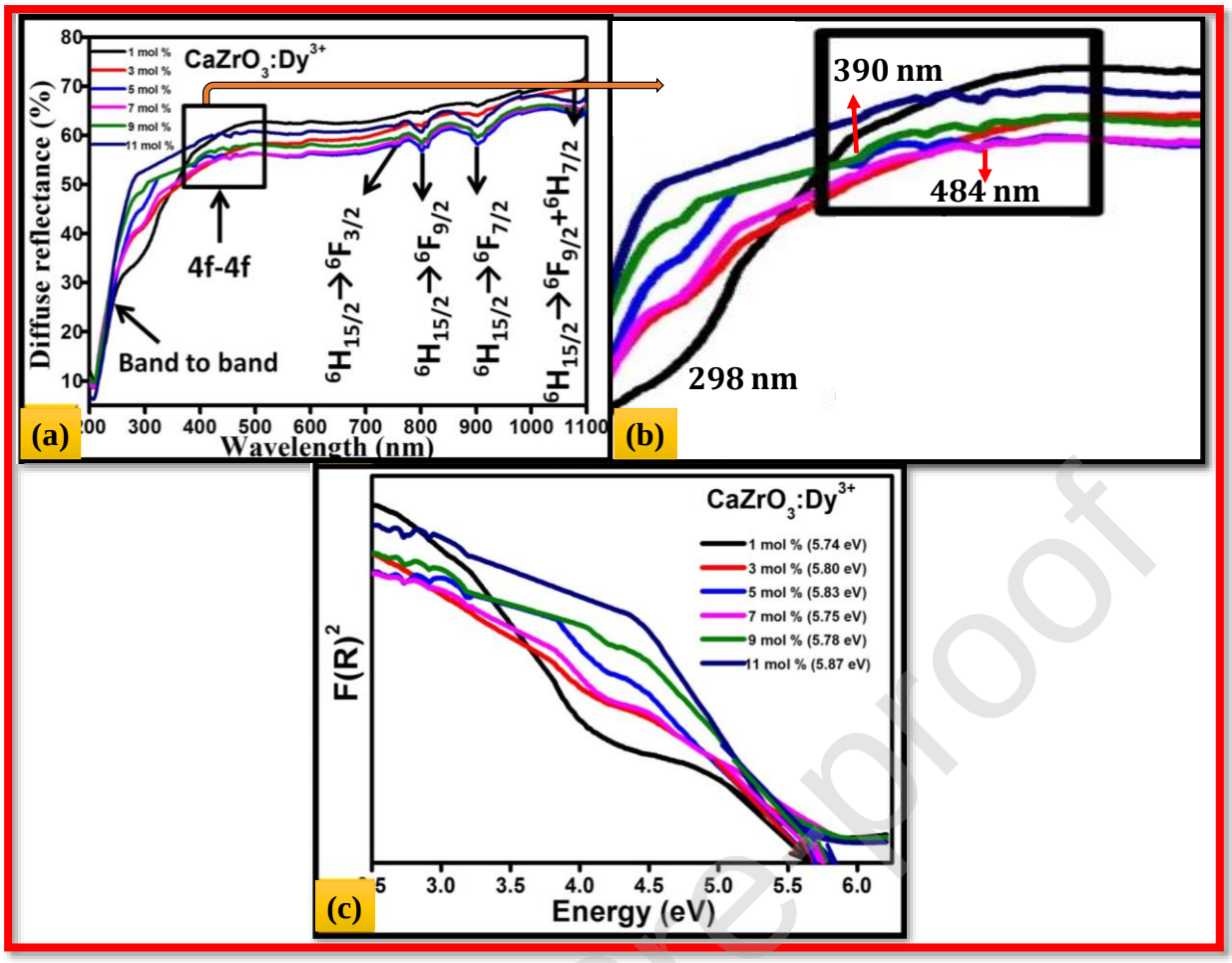

Fig.3 (a) DR spectra, (b) enlarged portion of DR spectra and (c) energy band gap plots of $CaZrO_3:Dy^{3+}$ (1-11 mol %) HS.

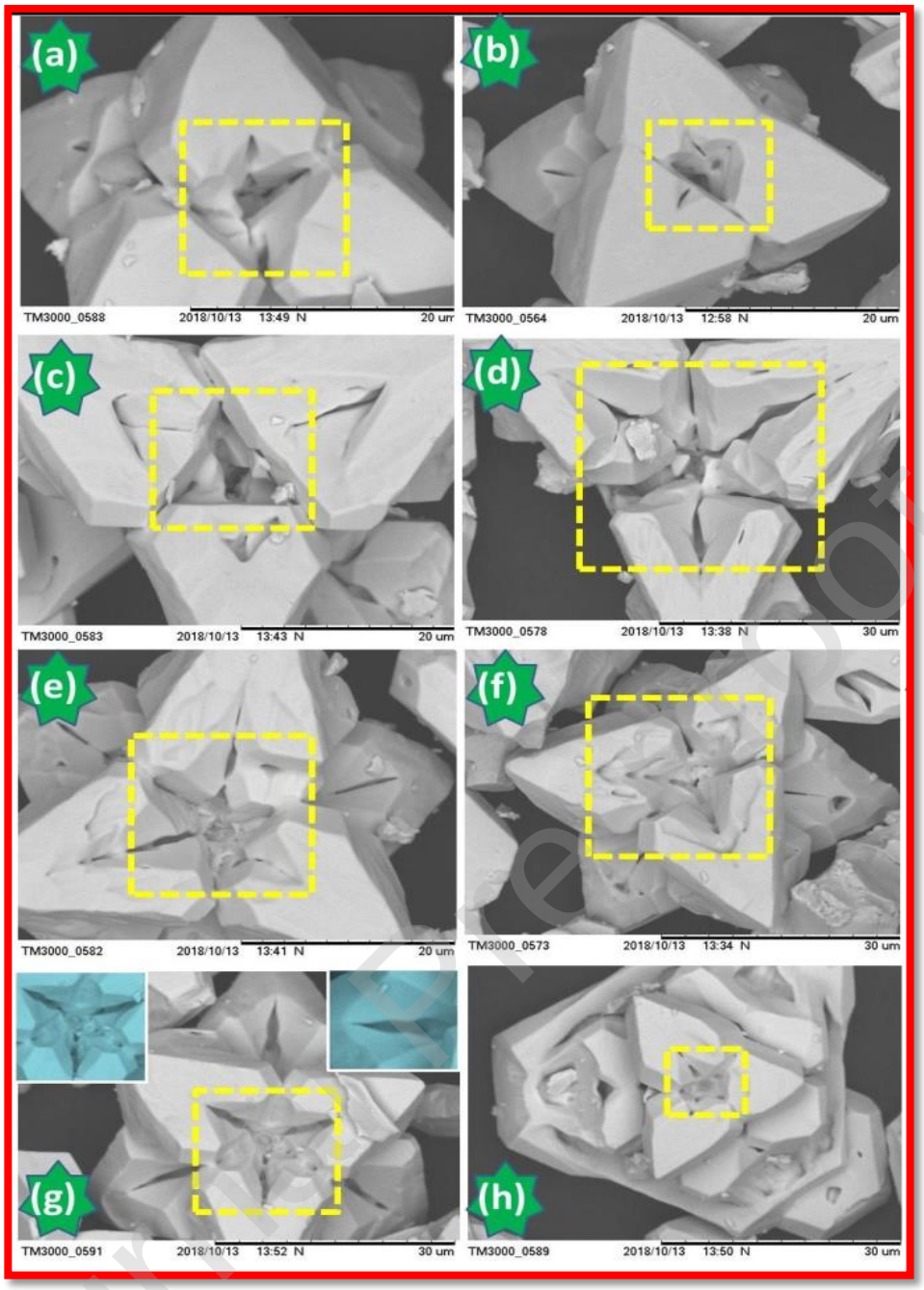

Fig.4. SEM micrographs of $CaZrO_3:Dy^{3+}$ (7 mol %) HS synthesized with different ultrasound irradiation time (1-8 h).

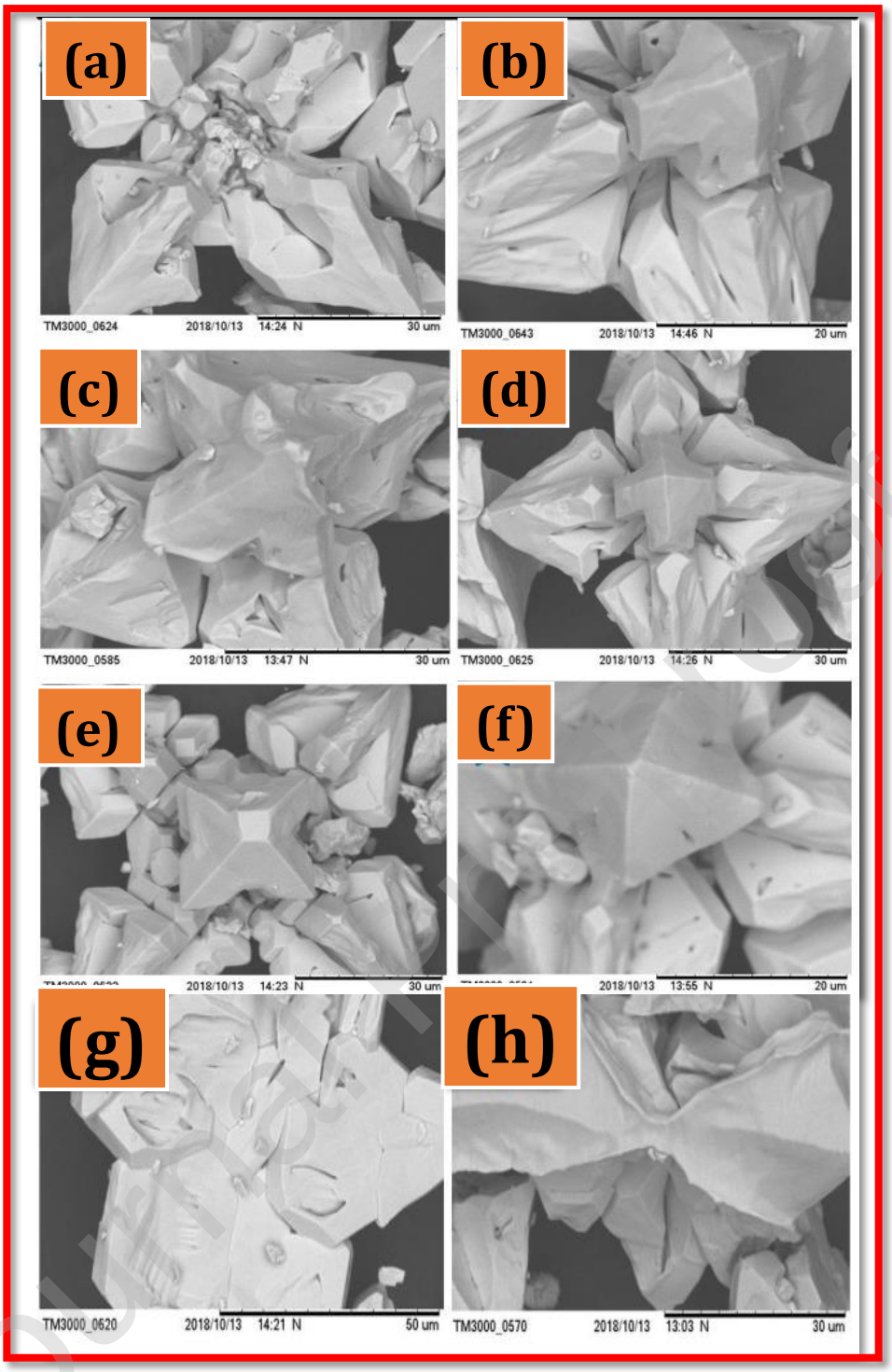

Fig.5. SEM micrographs of $CaZrO_3:Dy^{3+}$ (7 mol %) HS synthesized with (a-f) different *A. V.* gel concentration (5-30 mL) and (g & h) without ultrasound treatment.

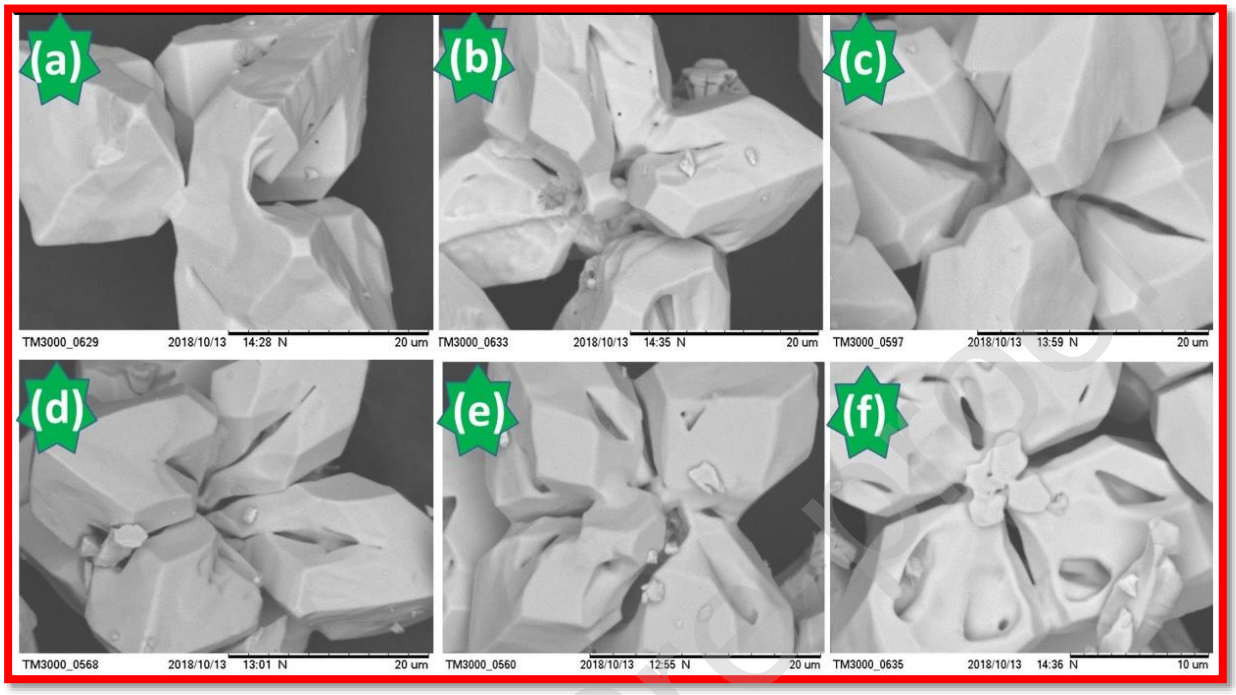

Fig.6. SEM micrographs of $CaZrO_3:Dy^{3+}$ (7 mol %) HS fabricated with different sonication power (20-30 kHz).

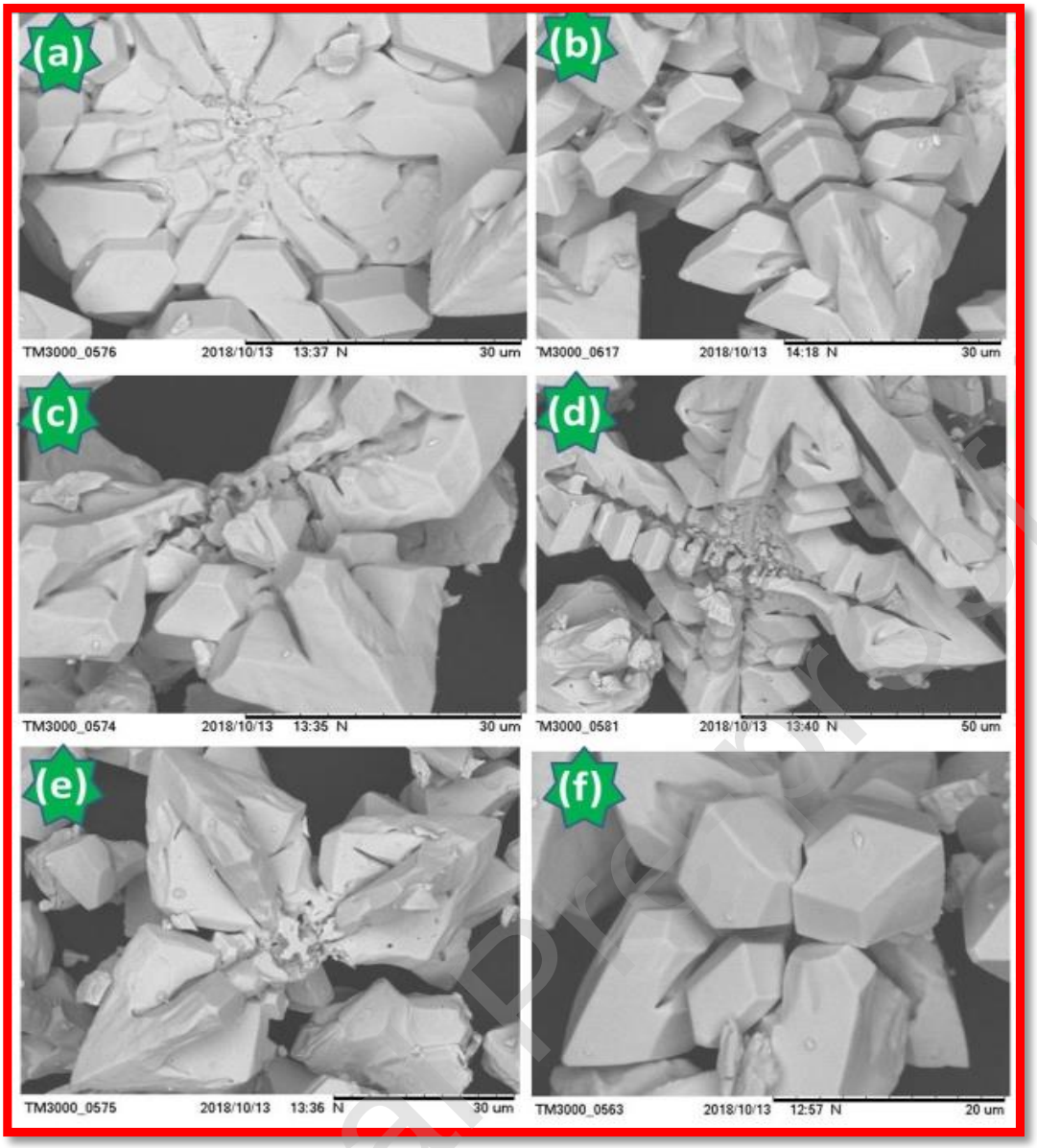

Fig.7. SEM micrographs of $CaZrO_3:Dy^{3+}$ (7 mol %) HS fabricated with different pH values (3-13).

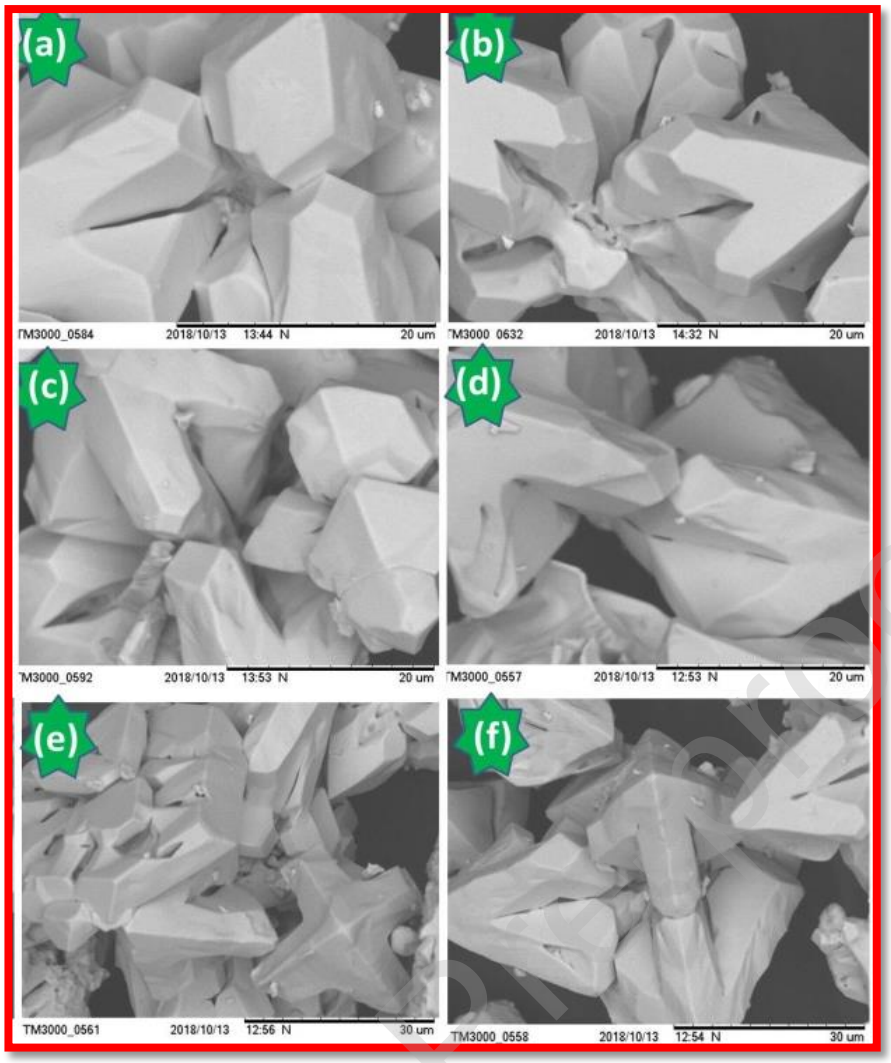

Fig.8. SEM micrographs of $CaZrO_3:Dy^{3+}$ (7 mol %) HS obtained with surfactant to water ratios (5-30 mL/30 mL).

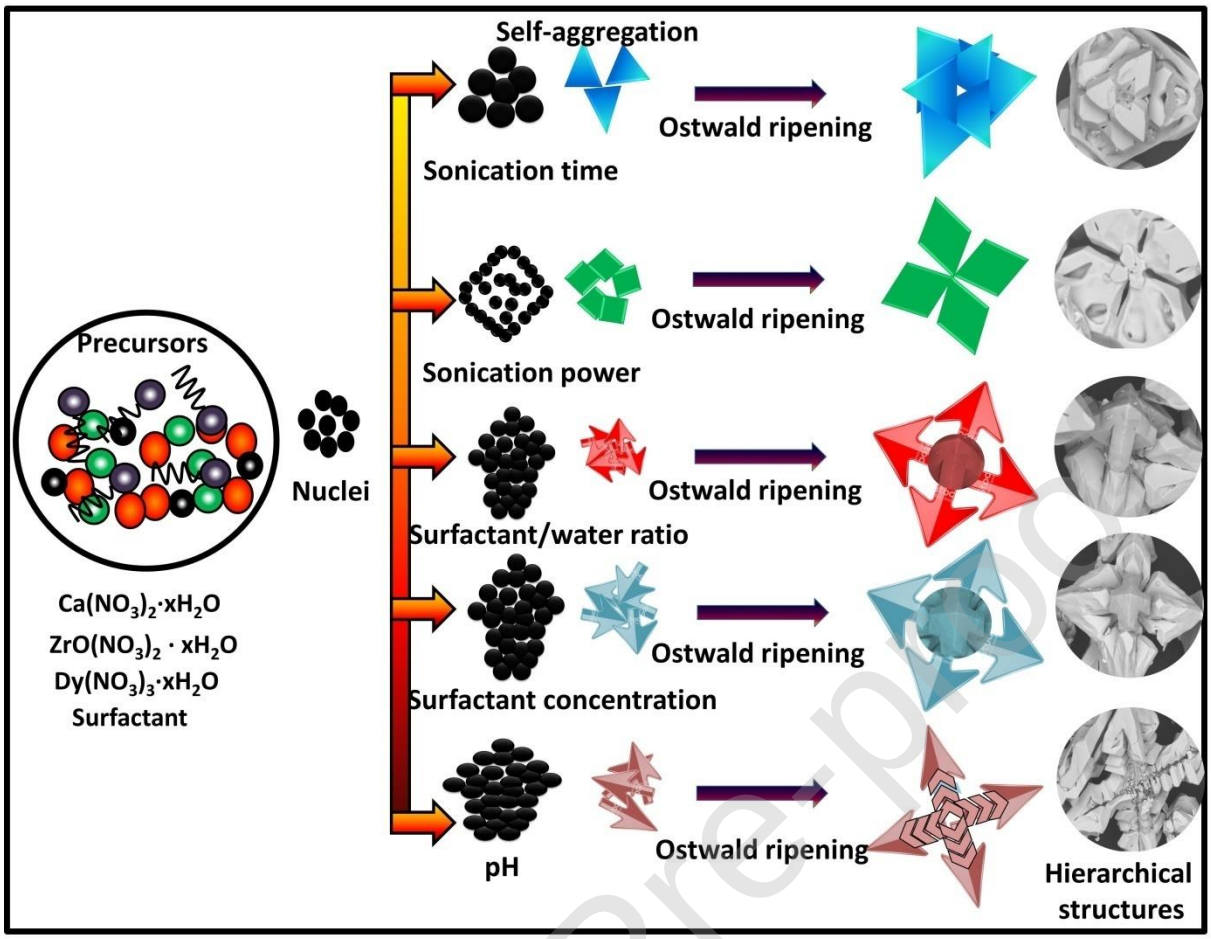

Fig.9. Possible growth mechanism for the formation of $CaZrO_3:Dy^{3+}$ (7 mol %) HS under various sonochemical reaction conditions.

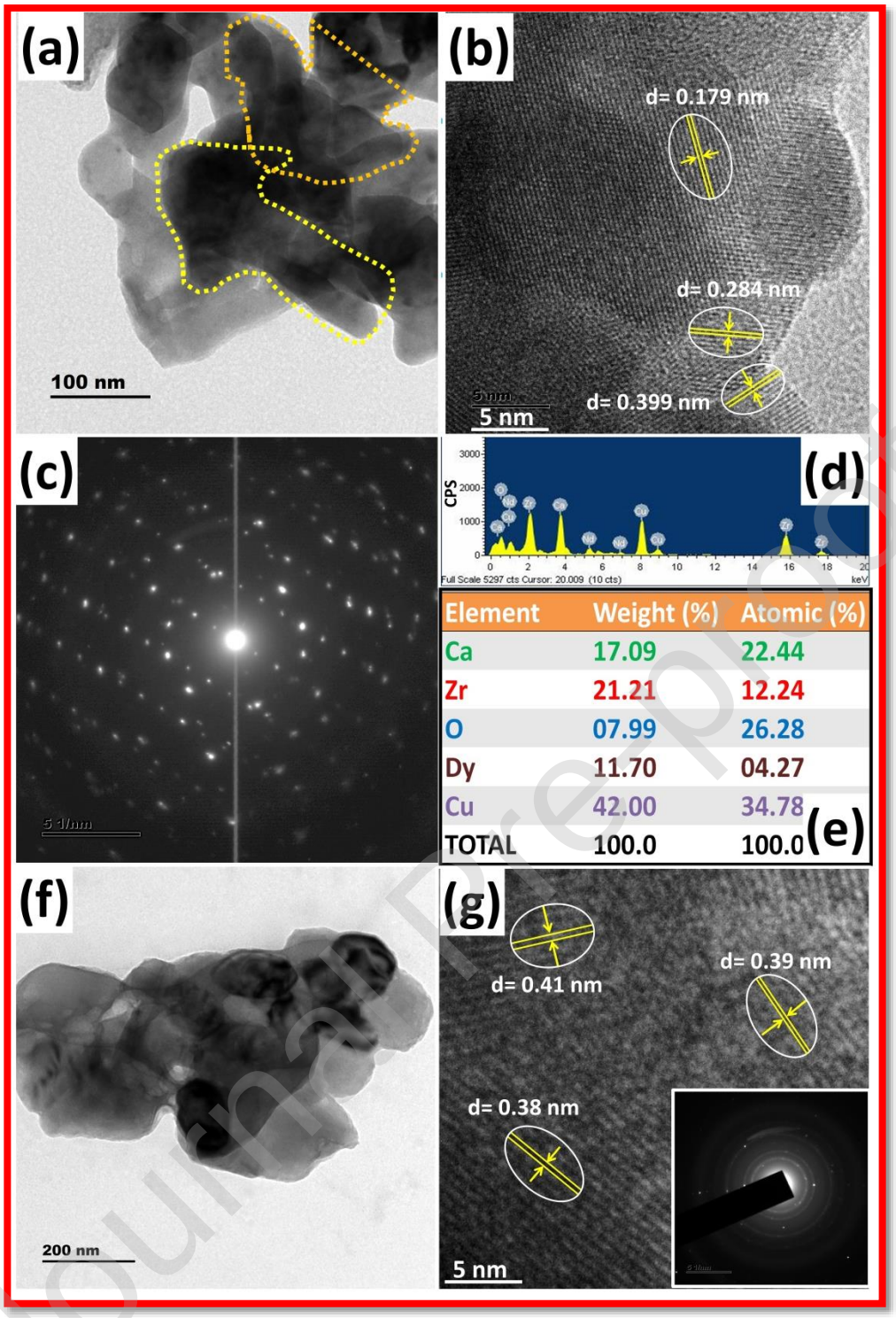

Fig.10 (a, b & c) TEM, HRTEM images, SAED patterns of ultrasonically prepared $CaZrO_3:Dy^{3+}$ (7 mol %) HS, (d, e) elemental analysis and composition table and (f, g) TEM and HRTEM images of mechanically stirred samples.

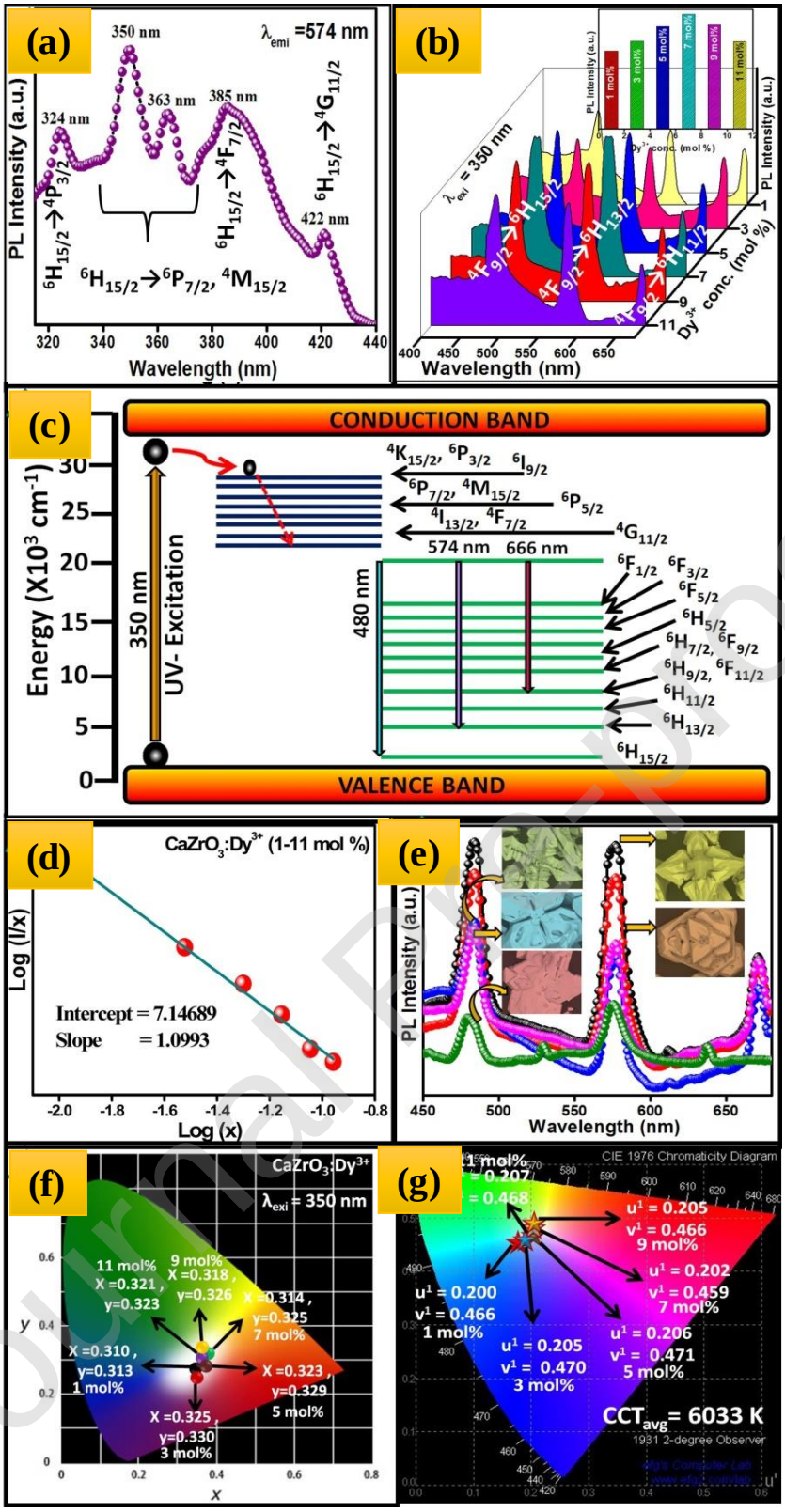

Fig.11 (a) PL excitation spectrum, (b) emission spectra (Inset: Plot of PL intensity v/s Dy^{3+} conc.), (c) energy level diagram of Dy^{3+} ions, (d) log (x) vs log (I/x) plot, (e) PL emission spectra with different sonochemical reaction parameters and (f & g) CIE and CCT diagrams of $CaZrO_3:Dy^{3+}$ (1-11 mol %) HS.

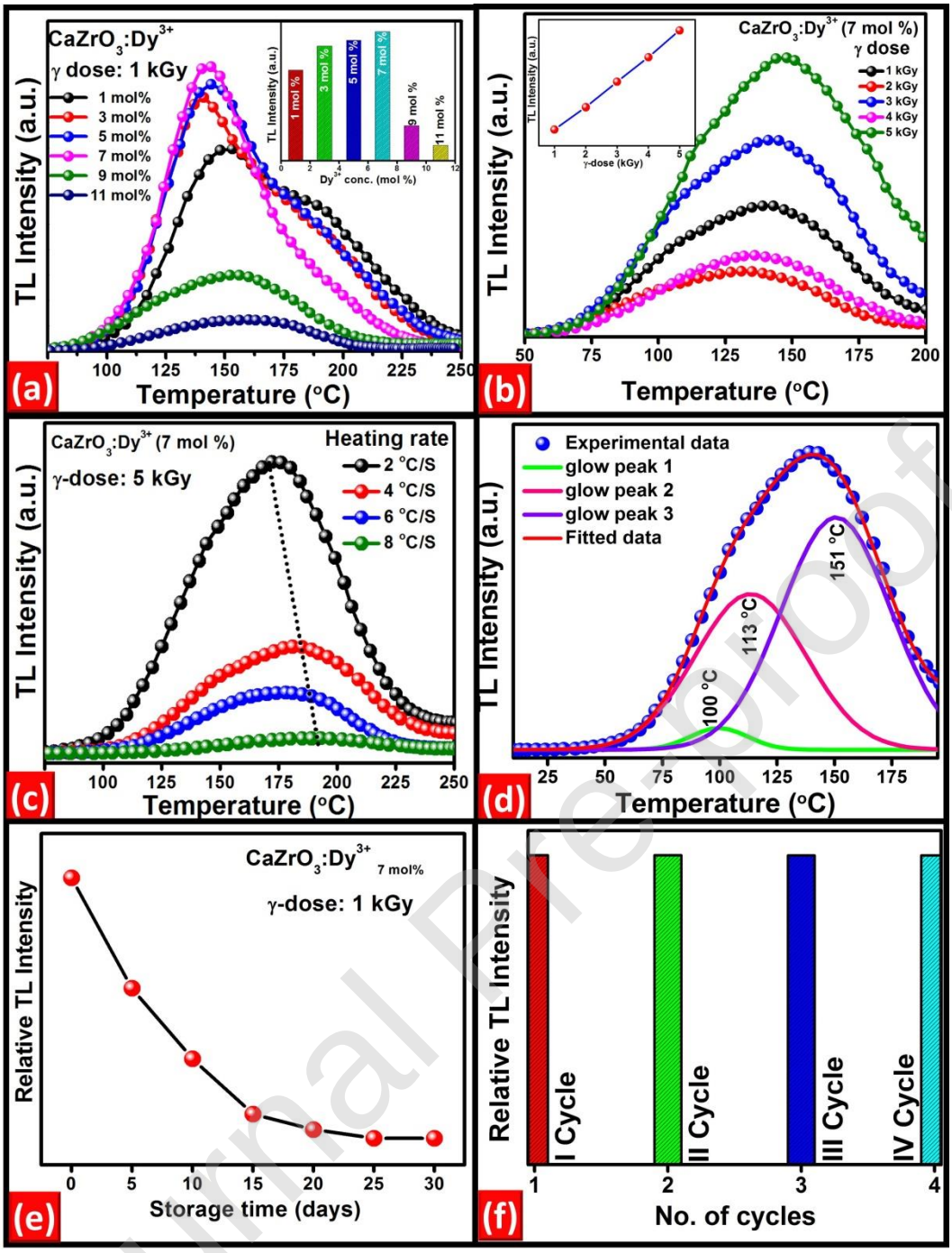

Fig.12 (a) TL glow curve of $CaZrO_3:Dy^{3+}$ (1-11 mol %) HS with 1 kGy γ-dose (Inset: TL intensity v/s Dy^{3+} concentration), (b) TL glow curve of $CaZrO_3:Dy^{3+}$ (7 mol %) HS with 1-5 kGy (Inset: TL intensity v/s γ-dose), (c) TL intensity of $CaZrO_3:Dy^{3+}$ (7 mol %) HS with different heating rate (2-8 °C/sec) and (d) Deconvoluted curve of $CaZrO_3:Dy^{3+}$ (7 mol %) HS with 2 °C/sec and (e & f) Fading and reproducibility characteristics of $CaZrO_3:Dy^{3+}$ (7 mol %) HS with 1 kGy γ-dose.

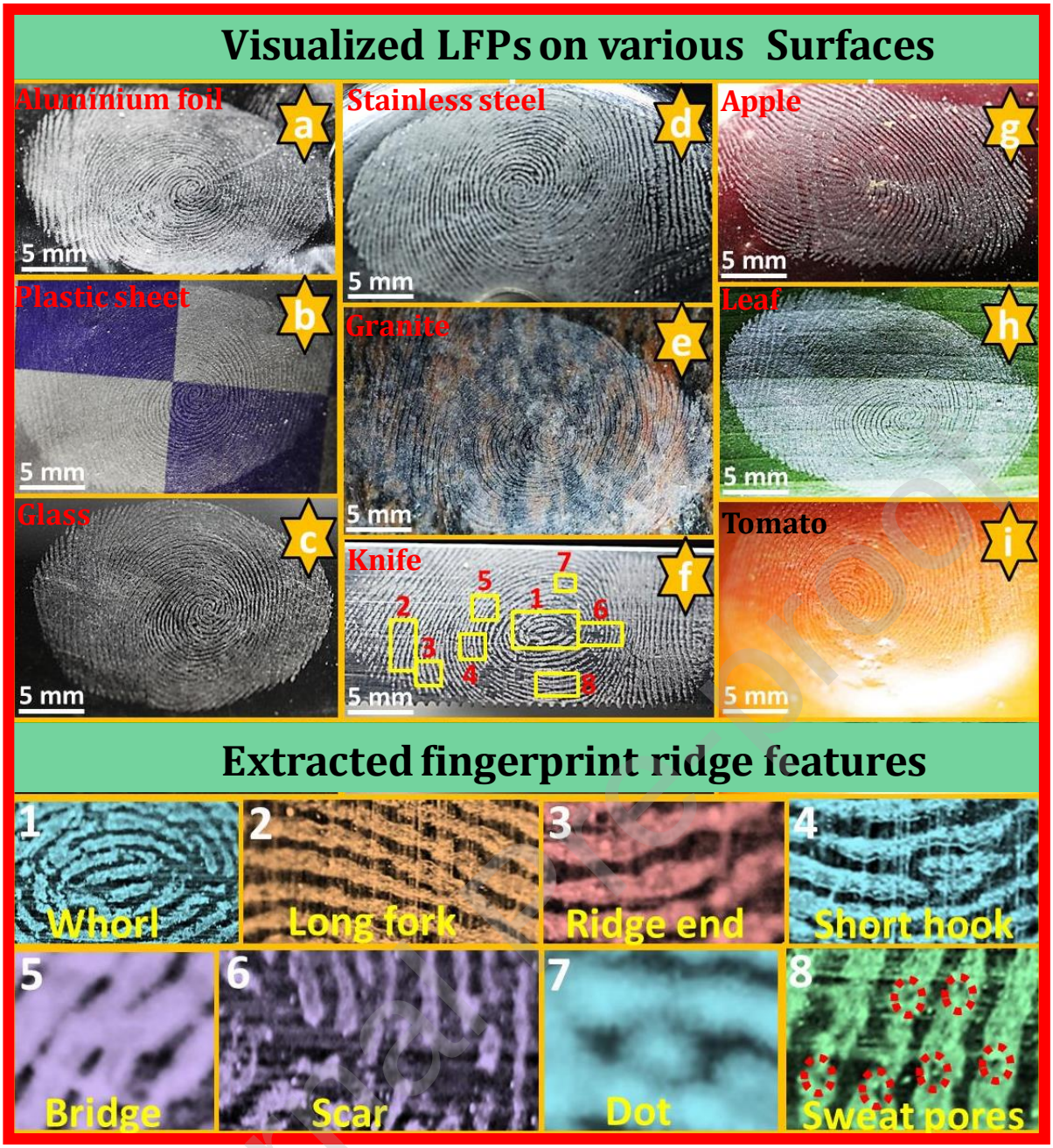

Fig.13. Visualized LFPs on porous (a-c), non-porous (d-f), semi-porous surfaces (g-i) and extracted ridge features on knife surface (1-9) using $CaZrO_3:Dy^{3+}$ (7 mol %) HS under normal light.

Table 1. The estimated average crystallite size, micro strain and energy gap values of $CaZrO_3:Dy^{3+}$ (1-11 mol %) HS.

Dy^{3+} conc. (mol %)	**Crystallite size (nm)**		**Micro strain (x 10^{-3})**	**Energy gap (eV)**
	Scherrer's method	**W-H plots**		
1	23	24	2.70	5.74
3	25	27	2.76	5.80
5	29	31	3.24	5.83
7	33	36	3.47	5.75
9	36	38	3.49	5.78
11	40	41	3.56	5.87

Table 2. Rietveld refined structural parameters of $CaZrO_3:Dy^{3+}$ (7 mol %) HS.

Atoms	**Oxidation State**	**Wyckoff notations**	**Atomic co-ordinates**			**Biso**	**Occupancy**
			x	***y***	***z***		
Ca	+2	(4c)	0.0252(2)	0.2612	−0.0556(2)	0.052	0.96
Dy	+3	(4c)	0.0253(2)	0. 2612	−0. 0556(2)	0.052	0.06
Zr	+4	(4a)	0.0000	0.0000	0.5000	0.052	1.00
O1	−2	(4c)	0.6523(7)	0. 2612	0.0015(5)	0.503	1.00
O2	−2	(8d)	0.2992(5)	0.0632(3)	0.2958(4)	0.503	1.00

Crystal system = Orthorhombic, Space group = *Pcmn* (No. 62); Lattice parameters: $a = 5.709(2)$(Å), $b = 8.930(2)$, $c = 5.378(4)$(Å); R factors(%): $R_p = 7.67$, $R_{wp} = 9.78$, $R_{exp} = 7.92$, $\chi^2 = 1.39$, $R_{Bragg} = 8.97$, $R_F = 9.92$.

Table 3. Photometric characteristics of $CaZrO_3$: Dy^{3+} (1- 11 mol %) HS.

Dy^{3+} conc. (mol %)	CIE		CCT		CCT (K)	CP (%)
	x	y	u'	v'		
1	0.321	0.323	0.200	0.466	6014	93
3	0.310	0.313	0.205	0.470	5980	94
5	0.325	0.330	0.206	0.471	6017	89
7	0.323	0.329	0.202	0.459	6210	96
9	0.314	0.325	0.205	0.466	5996	94
11	0.318	0.326	0.207	0.468	5984	92

Table 4. Summary of the activation energy (E), shape factor (μ), frequency factor (S) and average energy of the glow curve of $CaZrO_3:Dy^{3+}$ (1-11 mol %) HS with γ-dose (5 KGy).

γ-irradiation (5 KGy)								
Dy^{3+} conc. (mol %)	**Peak**	**T_m (°C)**	**b (μ_g)**	**Activation energy, E (eV)**				**Frequency factor, s (Hz)**
				E_τ	**E_δ**	**E_ω**	**E_{ave}**	
1	1	100	2(0.48)	0.150	0.143	0.262	1.332	2E+08
	2	113	2(0.49)	0.193	0.187	0.380	1.328	4E+08
	3	151	2(0.49)	0.181	0.174	0.355	1.384	3E+09
3	1	101	2(0.50)	0.144	0.143	0.287	1.367	1E+11
	2	114	2(0.51)	0.131	0.137	0.268	1.460	1E+11
	3	152	2(0.48)	0.187	0.174	0.362	1.315	7E+08
5	1	103	2(0.51)	0.811	0.873	0.168	1.565	6E+17
	2	114	2(0.50)	0.106	0.106	0.212	1.455	1E+14
	3	153	2(0.50)	0.218	0.218	0.436	1.303	1E+08
7	1	101	2(0.52)	0.749	0.811	0.156	1.679	7E+17
	2	112	2(0.50)	0.175	0.174	0.349	1.356	2E+09
	3	153	2(0.48)	0.119	0.112	0.230	1.458	7E+11
9	1	102	2(0.51)	0.125	0.131	0.255	1.449	1E+12
	2	112	2(0.51)	0.137	0.143	0.280	1.464	4E+10
	3	151	2(0.51)	0.874	0.936	0.181	1.751	1E+14
11	1	100	2(0.49)	0.169	0.162	0.330	1.321	9E+09
	2	113	2(0.48)	0.225	0.212	0.312	1.328	8E+09
	3	151	2(0.48)	0.125	0.118	0.243	1.446	2E+15

Table 5. Summary of the activation energy (E) values, shape factor (μ), frequency factor (S) and average energy of the glow curve for different γ doses of the $CaZrO_3:Dy^{3+}$ (7 mol %) HS.

γ-dose (KGy)	Peak	T_m (°C)	b (μ_g)	Activation energy, E (eV)				Frequency factor, s (Hz)
				E_τ	E_δ	E_ω	E_{ave}	
1	1	100	2(0.48)	0.262	0.243	0.505	1.251	4E+09
	2	113	2(0.51)	0.175	0.187	0.362	1.381	1E+09
	3	151	2(0.50)	0.144	0.143	0.287	1.431	2E+10
2	1	101	2(0.46)	0.144	0.124	0.268	1.275	5E+11
	2	114	2(0.50)	0.119	0.118	0.237	1.481	1E+12
	3	152	2(0.50)	0.106	0.106	0.212	1.575	2E+12
3	1	100	2(0.51)	0.112	0.118	0.230	1.463	2E+13
	2	112	2(0.50)	0.106	0.106	0.212	1.459	8E+13
	3	150	2(0.49)	0.250	0.243	0.493	1.275	3E+09
4	1	101	2(0.52)	0.999	0.112	0.212	1.533	3E+14
	2	113	2(0.50)	0.624	0.624	0.124	1.677	3E+21
	3	150	2(0.51)	0.106	0.112	0.218	1.508	4E+13
5	1	101	2(0.51)	0.811	0.873	0.168	1.565	6E+17
	2	112	2(0.50)	0.106	0.106	0.212	1.455	1E+14
	3	152	2(0.50)	0.218	0.218	0.436	1.303	1E+08

Table 6. Summary of the trap depth (E) values, frequency factor (S) and FOM of the glow curve of the $CaZrO_3:Dy^{3+}$ (7 mol %) HS estimated by various methods.

Heating rate (K/s)	T_m (K)	Trap depth (eV)			S (s^{-1})	FOM %
		Glow curve shape methods				
		Chen's	Grossweiner	Kivitis and Hagebeuk		
2	131	1.28	1.14	1.24	2E+13	1.74
4	182	1.92	1.37	1.54	4E+15	1.88
6	143	1.35	1.73	1.08	7E+09	1.24
8	172	1.93	1.88	1.14	5E+11	1.01